scientific reports

Check for updates

OPEN

Synthesis, in vitro, and in silico studies of 4-chlorophenyl-sulfonyl Indole based thiosemicarbazones as competitive α-glucosidase inhibitors

Iqra Naseer[1], Saeed Ullah[2], Zahra Batool[1], Mariya al-Rashida[3], Talha Islam[3], Ajmal Khan[4,6], Javid Hussain[5], Ahmed Al-Harrasi[6]✉, Zahid Shafiq[1]✉, Ahmed Mohamed Tawfeek[7] & Mohammad Shahidul Islam[7]✉

The urgent need for effective and novel solutions to address the rising global epidemic of diabetes mellitus (DM) has become a priority for researchers. This chronic ailment, with its alarming prevalence and life-threatening complications (neuropathy, retinopathy and nephropathy), necessitates novel therapeutic strategies. Herein we have synthesized a novel series of *N*-substituted indole-based thiosemicarbazone derivatives 5(a-y) and explored their potential as α-glucosidase inhibitors. All the compounds displayed excellent inhibitory potential with IC_{50} values in the range 5.38–59.20 µM, vastly outperforming the reference inhibitor acarbose (IC_{50} = 871.40 ± 1.24 µM). Molecular docking and molecular dynamics simulation were also conducted, which revealed strong binding interactions with the active site of the enzyme. Compound 5u emerged as the most effective α-glucosidase inhibitor, making it a strong lead for the development of novel antidiabetic therapeutics. To strengthen the SAR rationale and to gain mechanistic insights into the enhanced α-glucosidase inhibition, quantum chemical descriptors of the eight most active thiosemicarbazones (5a, 5 h, 5 m, 5n, 5s, 5t, 5u, 5w) were computed using DFT, highlighting their reactivity and stability from a theoretical perspective.

Keywords 4-chlorophenyl-sulfonyl indole, Glucosidase, In silico, Molecular docking, Kinetics

Diabetes is one of the most prevalent non-infectious diseases worldwide that is still on the rise[1]. Consequently, the treatment costs add a significant strain on a country's economy. In fact, diabetes mellitus ranks second only to ischemic heart disease in terms of economic burden[2]. Between 80 and 90% of diabetes cases are type 2 diabetes (T2DM)[2]. T2DM is characterized by hyperglycemia (increased blood sugar levels), which is caused by a progressive loss of normal insulin production[3]. Furthermore, it was shown that individuals with T2DM had a 15% higher chance of dying at a young age, and a roughly 20-year shorter life expectancy[4]. The prevalence of T2DM in teenagers is increasing in tandem with the growth in childhood obesity, and this trend is expected to continue[5]. These associated risks clearly underscore the severity of this disease. T2DM patients are more prone to develop neuropathy, retinopathy, and nephropathy, which lowers their quality of life and also raises medical care expenditures[6–8]. The World Health Organization has recognized T2DM as a major worldwide health concern. According to estimates from the International Diabetes Federation, the prevalence of diabetes, which was 10.5% in 2021, will rise to 11.3% by 2030 and 12.2% by 2040[9].

A comprehensive strategy that incorporates both behavioral and pharmaceutical interventions is necessary for T2DM to reduce complications and maintain a high quality of life[10]. The main focus of the pharmacological

[1]Institute of Chemical Sciences, Bahauddin Zakariya University, Multan 60800, Pakistan. [2]Department of Biology and Biochemistry, University of Houston, Houston, TX 77004, USA. [3]Department of Chemistry, Forman Christian College (A Chartered University), Lahore, Pakistan. [4]Department of Chemical and Biological Engineering, College of Engineering, Korea University, 145 Anam-ro, Seongbuk-gu, Seoul 02841, Republic of Korea. [5]Department of Biological Sciences and Chemistry, University of Nizwa, Nizwa, Oman. [6]Natural and Medical Sciences Research Centre, University of Nizwa, Birkat Al Mauz, PC 616P.O. Box 33, Nizwa, Sultanate of Oman. [7]Department of Chemistry, College of Science, King Saud University, P. O. Box 2455, Riyadh 11451, Saudi Arabia. ✉email: aharrasi@unizwa.edu.om; zahidshafiq@bzu.edu.pk; mislam@ksu.edu.sa

intervention is the inhibition of α-glucosidase, which controls the breakdown of carbohydrates[11–13]. It is an enzyme embedded in the membrane of the small intestine's epithelial cells[14]. α-glucosidase catalyzes the final step, which is the digestion of carbohydrates and influences blood glucose levels after meals, which are abundant in the gastrointestinal (GI) tract[15]. It stimulates postprandial hyperglycemia by hydrolyzing the terminal, non-reducing 1,4-linked glycosidic bond of poly and disaccharides, releasing monosaccharides[16]. This enzyme is crucial for the breakdown of carbohydrates in the digestive tract, which can lead to an increase in blood glucose levels if left unchecked[17,18]. By slowing down the rate at which carbohydrates are absorbed and preventing postprandial hyperglycemia, α-glucosidase inhibitors (AGIs) can reduce blood glucose levels[19]. Thus, the discovery of a novel class of α-glucosidase inhibitors is imperative[20,21].

Indoles constitue a large part of naturally occurring molecules, which highlights its significance in drug discovery[22]. The facile accessibility of ondole scaffold, its diverse reactivity, and wide-ranging pharmacological activities such as antibacterial[23], anti-inflammatory[24] and antidiabetic potential[25] has attracted considerable attention. Additionally, indole has been widely recognized as a promising pharmacophore for the development of α-glucosidase inhibitors. Various indole-based inhibitors are reported to have excellent inhibition potential[26–29].

Thiosemicarbazones are a class of compounds known for their diverse pharmacological properties[30–32], ranging from anti-oxidant[33], anti-inflammatory[34], anti-tumor[35] to antimicrobial[36] properties[37]. Condensing carbonyl moieties with thiosemicarbazide yields these compounds[38]. The thiourea-derived functional core (NH and CS) of thiosemicarbazones is believed to be responsible for the observed pharmacological profile[38]. They have recently gained attention because of their potential anti-diabetic properties. Thiosemicarbazone derivatives inhibit various other enzymes linked to diabetes, such as glycogen phosphorylase, aldose reductase (ALR2), aldehyde reductase (ALR1), α-glucosidase, dipeptidyl peptidase-4, and α-amylase, resulting in strong overall antidiabetic action[33,39–42].

An efficient strategy for discovering new drug like moleules is pharmacophore hybridization, which involves combining two or more pharmacophoric features into a single molecule to enhance its binding affinity and therapeutic efficacy[43,44]. Similar compounds have previously shown significant α-glucosidase inhibitory activity, prompting further exploration of their potential in diabetes treatment[45–49] (Fig. 1). Given the broad spectrum of anti-diabetic potential associated with the indole and thiosemicarbazone pharmacophores[37,50], our goal was to hybridize both scaffolds to discover a single molecular scaffold that could have enhanced inhibition potential against the enzyme α-glucosidase. In the current work, we have developed a series of *N*-substituted indole-based thiosemicarbazone derivatives **5(a-y)** by coupling *N*-substituted indole with different thiosemicarbazides and examined the inhibitory effects against α-glucosidase.

Results and discussion

Chemistry

In the first step, indole-3-carbaldehyde (1) was *N*-sulfonylated with 4-chlorobenzenesulfonyl chloride (2) in DCM, employing triethylamine and catalytic amount of DMAP. In the second step, the synthesis of thiosemicarbazones **5(a-y)** was carried out by the reaction of *N*-substituted indole 3-carbaldehyde (**3**) with respective thiosemicarbazides **4(a-y)** in an equimolar ratio in the presence of ethanol as solvent and acetic acid as a catalyst. The thiosemicarbazones **5(a-y)** were obtained as a solid residue in sufficient yield with excellent purity. The synthetic route for the synthesis of *N*-substituted thiosemicarbazones **5(a-y)** is displayed in Fig. 2.

All the synthesized compounds **5(a-y)** were characterized by ^{1}H and^{13}C NMR spectroscopy to confirm their structures. The presence of two singlets for NH protons at 12.26–11.50 ppm and 10.23–8.33 ppm and a singlet

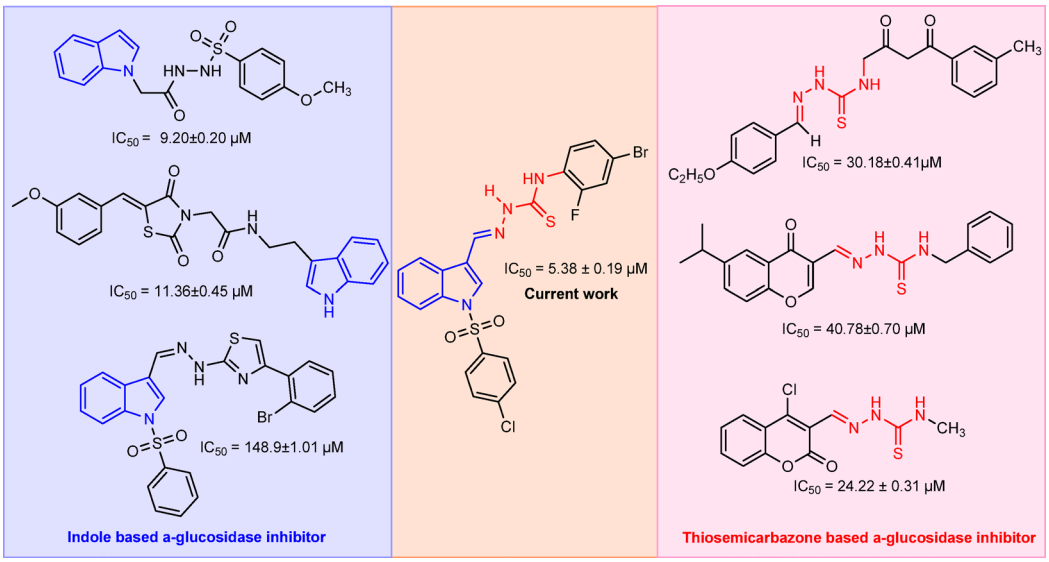

Fig. 1. Reported structures of α-glucosidase inhibitors based on indole and thiosemicarbazone, along with their respective IC_{50} values.

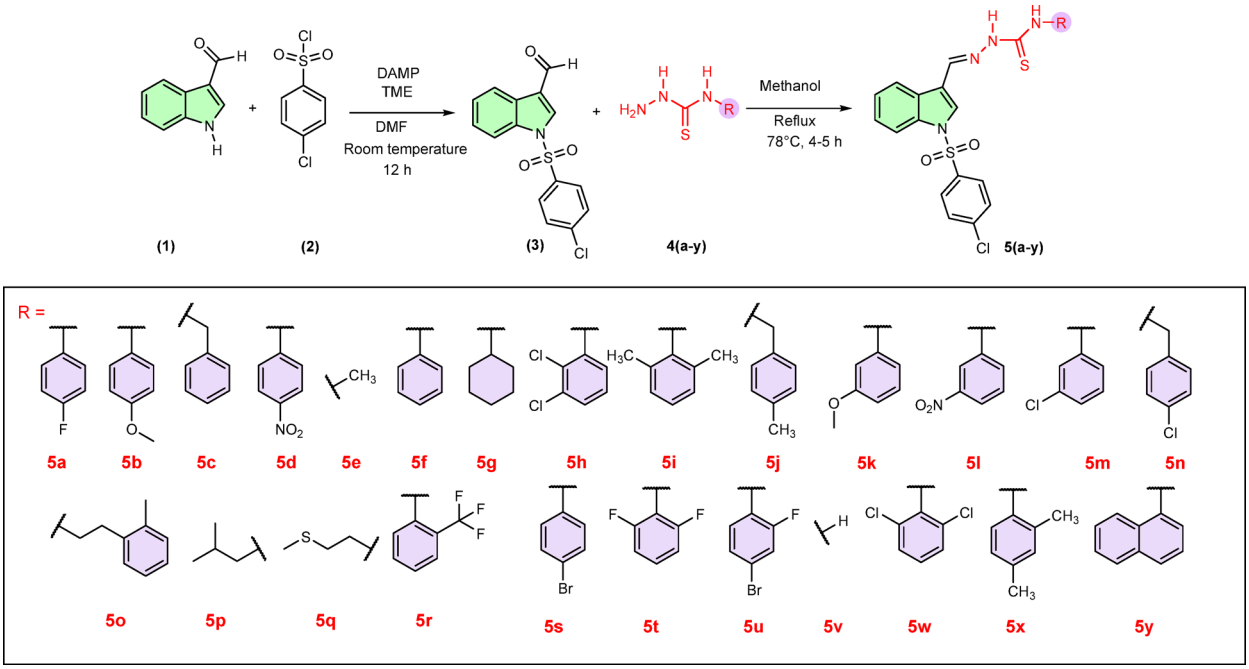

Fig. 2. Synthesis of thiosemicarbazone derivatives **5(a-y)**.

at 8.49–8.28 ppm for the azomethine proton in the ^{1}H NMR spectra of representative thiosemicarbazone **5(a-y)** suggests the successful condensation of thiosemicarbazide at the aldehyde group of indole. In the ^{13}C NMR, peaks at 178.16-176.02 ppm and 160.43-140.55 ppm are assigned to the C = S and OCH_3 / F substituted phenyl, respectively, which are consistent with our previously reported thiosemicarbazones[37].

α-glucosidase inhibition activity

Biological activity

All compounds **5(a–y)** were tested for their α-glucosidase in vitro inhibitory activity to explore their potential therapeutic applications. Interestingly, all compounds demonstrated strong inhibitory potency with IC_{50} values ranging from 5.38 ± 0.19–59.20 ± 1.60 µM, as displayed in Table 1. Compound **5u** was the most potent inhibitor and exhibited the highest inhibitory activity against α-glucosidase enzyme.

Structure activity relationship

A new class of *N*-substituted indole-based thiosemicarbazones has been synthesized and evaluated for its potential against the α-glucosidase enzyme. IC_{50} values and % inhibition of the synthesized compounds are displayed in Table 1. The effectiveness of this series of compounds is evident from the fact that all compounds in this series displayed excellent potential to inhibit α-glucosidase, with all compounds being 15–162 times more active than the standard inhibitor, acarbose. The inhibitory potential of the thiosemicarbazones is explored by changing the R group on the thiosemicarbazide moiety. The R group is varied with aromatic, non-aromatic, and aliphatic groups. These synthesized compounds **5(a-y)** exhibited slight variance in their IC_{50} values. The most active inhibitor **5u** was 162 folds potent than the standard inhibitor acarbose, while the least active inhibitor **5p** was fifteen folds more active than acarbose. Upon analyzing the potency landscape of all the inhibitors a gradual decrease in inhibition activity is observed (Fig. 3). This likely rules out the possibility that there is any specific single contact or a narrow set of contacts (hydrogen bond or hydrophobic) responsible for the observed biological activity. While the indole sulfonyl phenyl scaffold itself seems to be largely responsible for most of the "heavy-lifting", in terms of establishing key (and crucial) contacts with the binding site, the subtle differences or "fine-tuning" of inhibition activity can be attributed to the nature of R group.

This is also evident from the fairly narrow window (~ 11× from best to worst) reaffirming that the main chlorophenyl-sulfonyl indole scaffold is responsible for most of the interactions with the binding site, while R group substituent fine-tunes affinity via establishing secondary contacts (hydrophobic fit, edge-of-pocket polar contacts, and desolvation effects). Interestingly we observed that a variety of R groups (substituted phenyl, alkyl, cylo-alkyl and naphthyl) could be used without catastrophic loss of inhibition activity. The eight most active inhibitors all contained a halogenated phenyl ring, with **5u** being the most active inhibitor (IC_{50} = 5.38 ± 0.19 µM), closely followed by **5 h** and **5w** (having similar activity 6.39 ± 0.11 and 6.55 ± 0.17 µM, respectively). Compounds **5u**, **5 h**, **5w**, and **5s** are more than 100 folds active than acarbose. Figure 4 provides visual illustration of SAR trends observed herein.

Among the R group substituents, the alkyl chains seem to be less tolerated, as the compounds that were least active in the series (albeit still much more active than acarbose) were the ones containing 2-butyl (**5p**), naphthyl (**5y**), methyl (**5e**), 1-ethyl-2-methylphenyl (**5o**), thiopropyl (**5q**) and cyclohexyl (**5 g**) groups. These least active

S. no	Code	Inhibition percentage (0.5 mM)	IC_{50} = [value] ± [SEM] µM
1.	**5a**	91.00	10.66 ± 0.31
2.	**5b**	90.44	14.70 ± 0.35
3.	**5c**	83.16	35.22 ± 1.20
4.	**5d**	88.77	18.50 ± 0.48
5	**5e**	76.33	52.30 ± 1.40
6	**5f**	84.52	29.60 ± 0.83
7	**5 g**	80.74	41.26 ± 1.15
8	**5 h**	91.78	6.39 ± 0.11
9	**5i**	87.51	24.08 ± 0.37
10	**5j**	87.59	27.10 ± 0.53
11	**5k**	88.97	20.47 ± 0.51
12	**5 L**	90.05	16.11 ± 0.39
13	**5 m**	90.42	13.60 ± 0.27
14	**5n**	91.36	10.28 ± 0.25
15	**5o**	78.33	49.35 ± 1.40
16	**5p**	75.93	59.20 ± 1.60
17	**5q**	77.36	45.11 ± 0.82
18	**5r**	88.73	23.15 ± 0.27
19	**5s**	91.77	8.19 ± 0.15
20	**5t**	91.48	9.10 ± 0.26
21	**5u**	92.20	5.38 ± 0.19
22	**5v**	79.25	30.26 ± 0.64
23	**5w**	91.69	6.55 ± 0.17
24	**5x**	83.75	21.44 ± 0.38
25	**5y**	76.40	54.66 ± 1.13
Acarbose			871.40 1.24

Table 1. The enzyme Inhibition results in novel compounds **5(a-y)** against α-glucosidase.

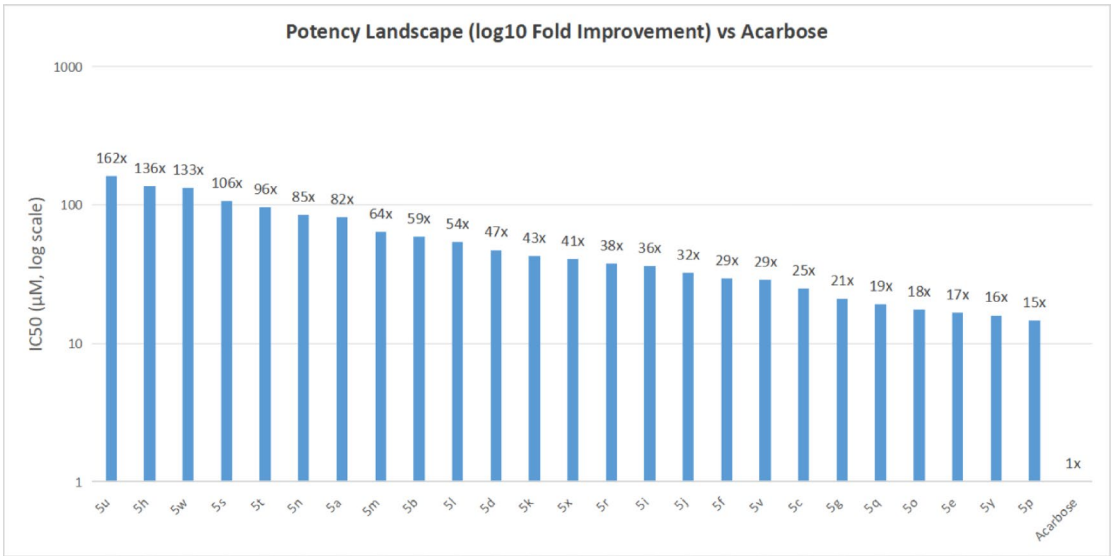

Fig. 3. Potency landscape of synthesized compounds compared to the standard inhibitor acarbose. IC_{50} values (µM, log scale) are shown for each compound, with fold-improvement in potency relative to acarbose indicated above each bar.

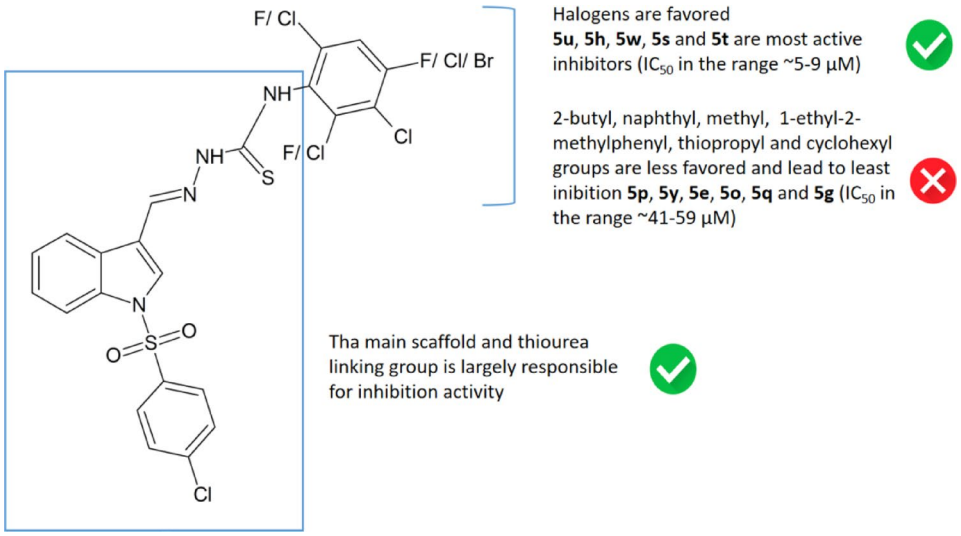

Fig. 4. SAR illustration of newly synthesized compounds **5(a-y).**

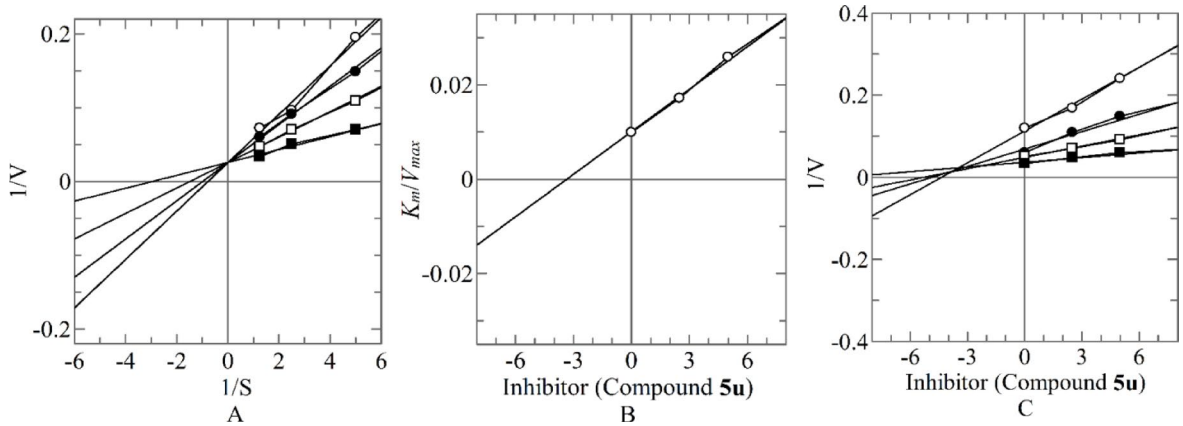

Fig. 5. The inhibition of α-glucosidase by compound **5u** (**A**) Line weaver-Burk plot of reciprocal of rate of reaction (velocities) vs. reciprocal of substrate concentration in the absence of (▪), and in the presence of 10.00 µM (○), 5.00 µM (●), and 2.50 µM (□) of compound **5u**. (**B**) Secondary replot of the Line weaver-Burk plot between the slopes of each line on the Line weaver-Burk plot vs. different concentrations of compound **5u**. (**C**) Dixon plot of the reciprocal of the rate of reaction (velocities) vs. different concentrations of compound **5u**.

compounds are still 15–20 folds active than acarbose. The nitro, methoxy, phenyl ring substituted with methyl groups and trifluoromethyl groups gave intermediate activity.

Enzyme kinetics study

The most potent compound, **5u**, was subjected to a mechanistic study to reveal its mechanism of action. The mechanism of action studies are crucial in drug discovery. Interestingly, we identified compound **5u** as a competitive type inhibitor with a K_i value of 3.57 ± 0.0084 µM. Such a type of inhibitor binds with the active site residues, thus increasing the K_m value while the V_{max} of the enzyme α-glucosidase remains constant (Fig. 5).

Molecular docking

The crystal structure of **α**-glucosidase enzyme from *S. cerevisiae* is not available from the PDB, hence, its homology model was built and validated as reported previously by us[51]. The oligo-1,6-glucosidase from *S. cerevisiae*, having PDB ID 3A4A, was found to be the best match and was used as a template for the homology modeling. Amino acids Asp214, Glu276, and Asp349 are part of the catalytic triad of the active site; interactions with these amino acids are critical for substrate binding. Similarly, the inhibitor's interaction with these amino acids is also deemed necessary for effective enzyme inhibition. In addition, amino acids Phe231, His239, Asn241, His279, Glu304, and Arg312 near the active site are also important for binding.

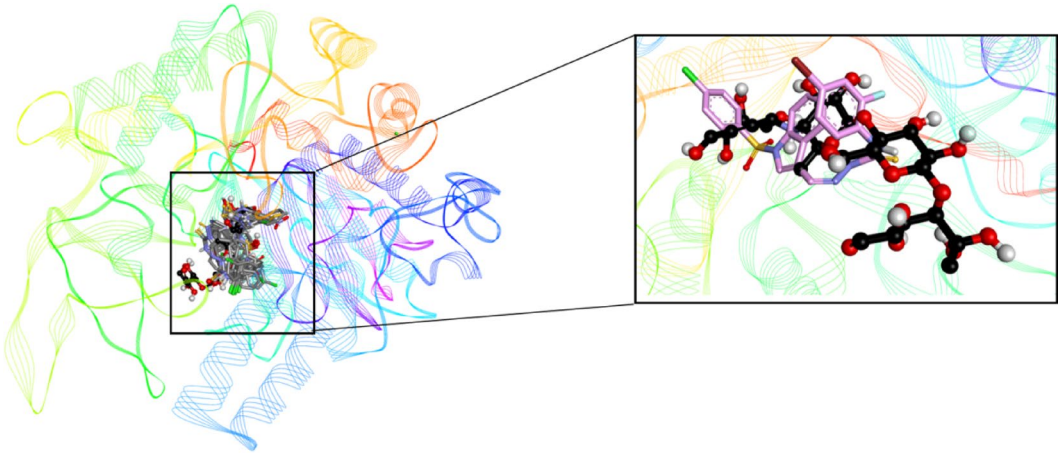

Fig. 6. Overlap of docked conformations of compounds **5(a-y)** with acarbose (black). The zoomed in region shows overlap of most active inhibitor **5u** with acarbose.

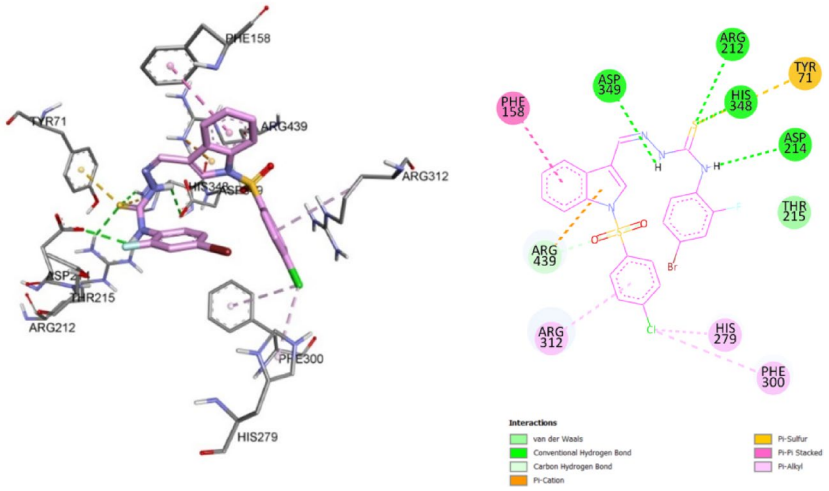

Fig. 7. Docked conformation of **5u** with α-glucosidase showing binding site interactions.

Molecular docking of all the compounds **5(a-y)** was carried out; for reference, acarbose, the standard inhibitor, was also docked (docking score = -13). All the compounds were found to be oriented in the same area of the active site as the standard acarbose. Figure 6 shows the overlap of all compounds with acarbose.

For the most active compound **5u**, the docking studies revealed a number of hydrogen bonded interactions that contribute to the stability of binding. The NH groups were making hydrogen-bonded interactions with Asp214 and Asp349, while the sulfur atom of the thiocarbonyl group was making a hydrogen bond with Arg212 and His348; the same sulfur atom was also making pi-sulfur interactions with Tyr71 and His348. One of the sulfonamide group oxygen atoms was making a carbon-hydrogen bond with Arg439. The indole ring was making a pi-pi stacked interaction and a pi-cation interaction with Phe158 and Arg439, respectively. The chlorophenyl ring was making a pi-alkyl interaction with Arg312, and the chlorine atom was making pi-alkyl bonds with Phe300 and His279.

Docking studies were also carried out for compounds **5w** and **5 h**, also having excellent inhibition activities ($IC_{50} = 6.55 \pm 0.17$ µM and 6.39 ± 0.11 µM, respectively) Fig. 7. As expected, similar interactions were observed (Table 2). All three compounds form hydrogen bonds with arginine (Arg) residues. Arg439 is involved in pi-Cation interactions in both **5u** and **5w**. Glu276 is involved in Pi-Anion interactions in both **5w** and **5 h**. Asp349 is involved in pi-Anion interactions in **5w**, but in **5u**, it forms a hydrogen bond instead. Tyr71 is involved in pi-pi interactions in both **5w** and **5 h**. Pi-Sulfur interactions are observed in **5w** and **5 h**, but not in **5u**. Chlorine is involved in pi-Alkyl interactions in all three compounds. Arg312 and Arg439 are involved in pi-Alkyl interactions in **5u** and **5 h**, and **5w**, respectively.

To better understand the differences between the most active (**5u**) and least active inhibitor (**5p**), docked conformations of both were compared. It has already been established during SAR studies that the main sulfonyl indole scaffold is largely responsible for the inhibition activity, by providing key anchoring with the amino acids

Interaction	Category	Distance (Å)
Compound 5u (docking score = -11)		
ARG212:HH11 - lig: S24	Hydrogen bond	2.83
HIS348:HE2 - lig: S24	Hydrogen bond	2.83
lig: H44 - ASP349:OD2	Hydrogen bond	2.87
lig: H45 - ASP214:OD1	Hydrogen bond	3.08
THR215:HB - lig: F33	(Carbon) Hydrogen bond	1.64
HIS279:HE1 - lig: Cl17	(Carbon) Hydrogen bond	3.03
ARG439:NH1 – lig	Electrostatic Pi-Cation	3.13
lig: S24 - TYR71	Other	3.83
lig: S24 - HIS348	Other	4.89
PHE158 – lig	Pi-Pi stacked	4.35
HIS279 - lig: Cl17	Pi-Alkyl	4.21
PHE300 - lig: Cl17	Pi-Alkyl	4.47
lig - ARG312	Pi-Alkyl	4.83
Compound 5w (docking score = -10.82)		
ARG212:HH22 - lig: O18	Hydrogen bond	2.86
lig: H45 - PHE157:O	Hydrogen bond	1.97
ARG439:NH1 – lig	Pi-Cation	4.96
ARG439:NH1 – lig	Pi-Cation	3.04
GLU276:OE2 – lig	Pi-Anion	3.47
GLU276:OE2 – lig	Pi-Anion	3.65
ASP349:OD1 – lig	Pi-Anion	4.08
ASP408:OD2 – lig	Pi-Anion	2.69
lig: S24 - PHE157	Pi-Sulfur	4.71
TYR71 – lig	Pi-Pi stacked	4.08
lig – lig	Pi-Pi stacked	4.71
TYR71 - lig: Cl17	Pi-Alkyl	4.87
lig - :ARG439	Pi-Alkyl	5.40
Compound 5 h (docking score = -10)		
ARG439:HH12 - lig: O19	Hydrogen bond	1.82
ARG312:HD2 - lig: Cl33	(Carbon) Hydrogen bond	2.25
ARG439:HD2 - lig: O19	(Carbon) Hydrogen bond	2.23
ARG312:NE - lig: Cl33	Halogen	3.02
GLU276:OE2 – lig	Pi-Anion	4.04
GLU276:OE2 – lig	Pi-Anion	3.48
lig: S24 – lig	Pi-Sulfur	5.99
TYR71 – lig	Pi-Pi T-shaped	5.19
lig – lig	Pi-Pi T-shaped	5.39
TYR313 - lig: Cl17	Pi-Alkyl	5.14
lig - ARG312	Pi-Alkyl	5.47
lig - ALA278	Pi-Alkyl	5.43

Table 2. Binding interactions of the most active inhibitor **5u**, **5w**, and **5 h**.

of the binding site, the "fine-tuning" and hence better inhibition of **5u** compared to **5p** (about 11 folds) appears to be due to the difference in the R group. Several factors may account for this, including physiologically relevant effects such as solvent displacement and water-mediated interactions with additional amino acid residues. Within the limitations of the static view provided by molecular docking, we observed that compared to **5u**, in **5p** only the sulfur atom of the thiocarbonyl group was engaged in hydrogen-bonded interactions with His111 and Gln181, whereas in **5u** the same sulfur atom was making two additional hydrogen bonds with Arg212 and His348. While the adjacent (hydrophobic) butyl group engaged the nearby amino acids in hydrophobic contacts, this part of the molecule significantly lacked polar interactions (Fig. 8).

Similarly, we decided to compare related compounds **5b** (containing a 4-methoxyphenyl group) and **5k** (containing a 3-methoxyphenyl group) that differ only in the position of the methoxy substituent on the phenyl ring (Fig. 9). Not much difference in their activity was observed; in fact, compound **5b** was only 1.3 folds more active than **5k**. Pi-sulfur interactions with His245 and Phe157 were observed with the sulfur atom of the thiocarbonyl group in compounds **5b** and **5k**, respectively. The sulfonamide oxygen in both compounds was making hydrogen bonds with Arg439 and Arg212, respectively. Similarly, the indole rings were stabilized

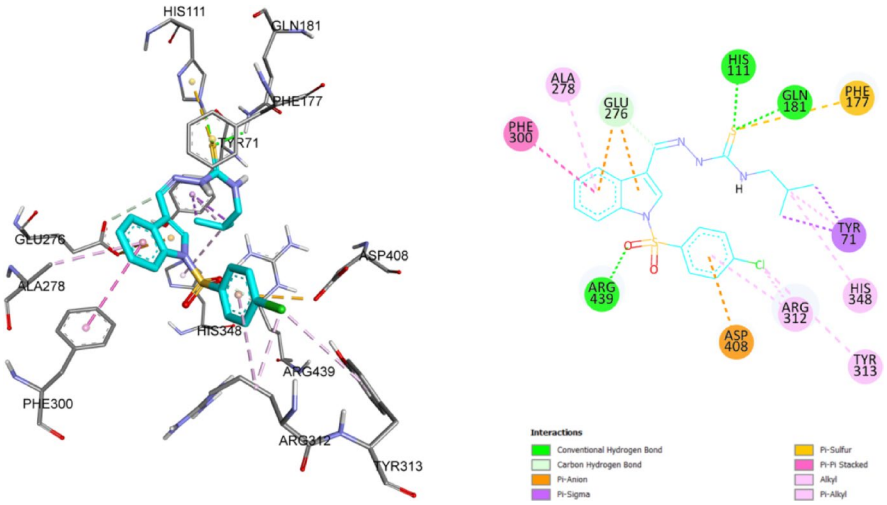

Fig. 8. Docked conformation of **5p** with α-glucosidase showing binding site interactions.

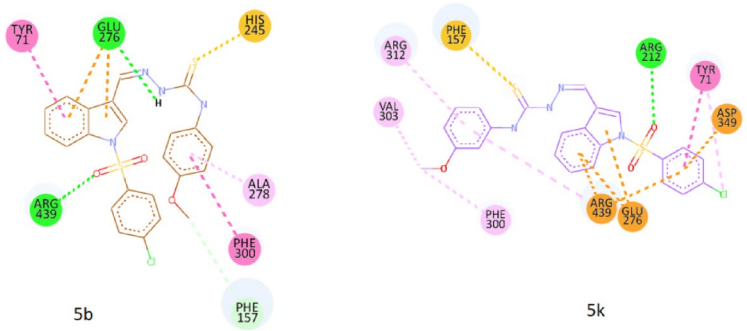

Fig. 9. Comparison of 2D docked conformation of inhibitors **5b** and **5k**.

through a network of electrostatic (pi-cation and pi-anion) interactions with Glu276, Arg439, and Asp349 in both compounds. Tyr71 was making a pi-pi stacked interaction with the indole ring of **5b** and the chlorophenyl ring of **5k**. The methoxyphenyl ring in **5k** was stabilized only via a network of pi-alkyl interactions with Arg312, Arg439, Val303, and Phe300. In contrast, the methoxy group of **5b** was making a carbon-hydrogen bond with Phe157, while its phenyl ring was making a pi-alkyl and pi-pi stacked interaction with Ala278 and Phe300, respectively. The only other additional interaction found in **5b** was a hydrogen bond between the NH group and Glu276, which was absent in **5k**.

Molecular dynamics (MD) simulation studies

The Molecular Dynamics Study of **5u**-α-glucosidase Complex showed that the C-α Protein RMSD increased from 1.5 Å to 2.1 Å in the initial 50 ns, then the value ascended slightly up to 2.7 Å for the next 20 ns and remained stable around 2.4 Å with minor fluctuations and at 2.6 Å at the end of the simulation period. In the **5u** RMSD graph, the Lig fit on Protein value increased from 1.3 Å to 4 Å in the first 25 ns, then decreased and remained stabilized around 2.5 Å for the next 75 ns (till 100 ns), then in the last 50 ns, the value fluctuated and remained around 4.2 Å towards the end of the simulation period. The Lig fit on Lig RMSD value remained stabilized around 0.6 Å in the initial 100 ns, then fluctuated around 2.1 Å in the last 50 ns of simulation Fig. 10.

Protein RMSF analysis showed all residues of α-glucosidase that made contact with **5u** showed RMSF values less than 2.0 Å, where relatively higher values were shown by residues around number 230 (up to 5.8 Å), 420 (up to 4.1 Å), and 550–570 (up to 4.0 Å and 3.5 Å respectively) towards the C-terminal. Relatively higher RMSF values were shown by residues in the loop regions in the protein overall. Ligand fit on the Protein RMSF graph showed most atoms of **5u** showed values less than 2.0 Å in fluctuations, except the bromofluorobenzene moiety at around 5 Å.

The Molecular Dynamics Simulation of **5u** with α-glucosidase showed that the complex remained relatively stable during the 150 ns simulation time, as the protein RMSD value was observed below 3.0 Å during the whole simulation time. Nevertheless, values of **5u**'s RMSD and simulation trajectory visual analysis revealed the change in the conformation of **5u**. At the same time, the position and orientation of **5u** remained comparatively stable in the active site of α-glucosidase during the whole simulation. This is also corroborated by the superimposed images of 5u at different time intervals in the simulation (Fig. 11).

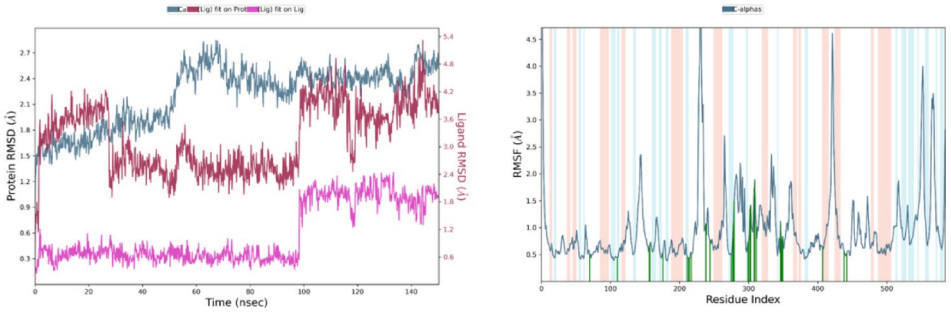

Fig. 10. RMSD and protein RMSF graphs of **5u**-α-Glucosidase complex for 150 ns simulation.

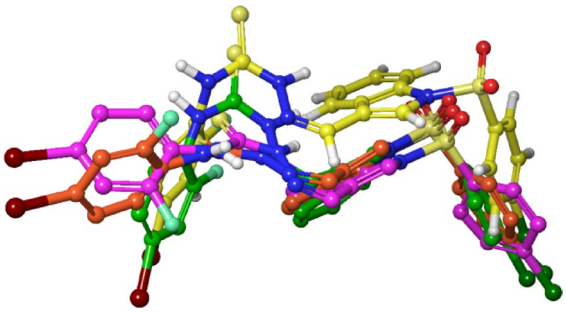

Fig. 11. Superimposed structure poses of **5u** during simulation at different time intervals, Yellow at 0 ns, Green at 30 ns, Magenta at 100ns, and Orange-red at 150 ns, respectively.

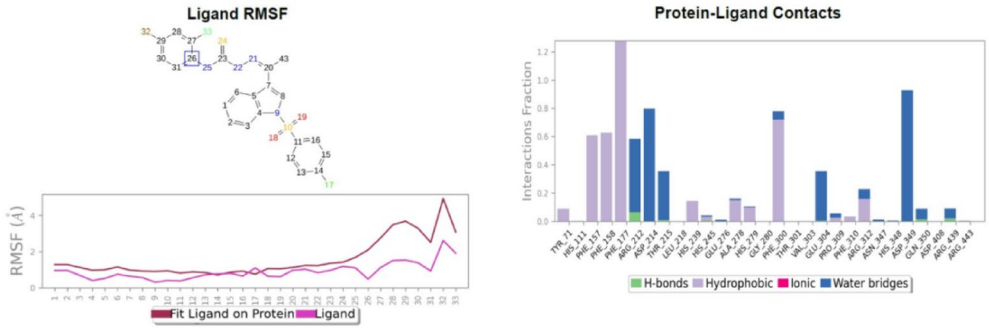

Fig. 12. Ligand RMSF and protein-ligand contacts, of inhibitor **5u** with α-glucosidase during the simulation.

Protein Secondary Structure elements revealed % Total SSE = 38.60, where % α-helices = 22.58 and % β-strands = 16.02. Protein-Ligand contacts exhibited that a maximum interaction fraction of above 1.2 was exhibited by *Phe 177*, *which* contained mostly hydrophobic interactions, while other residues mostly showed water bridges and hydrophobic interactions. Ligand-protein contacts reveal that *Asp 214* maintained a water-mediated charged interaction with the sulfur dioxide moiety at 79% of simulation time. *Phe 177* showed Pi-Pi stacking interaction with indole and chlorobenzene moiety at 46% and 32% respectively, and *Phe 300* showed Pi-Pi stacking interaction with indole ring at 50%. *Asp 349* and *Arg 212* maintained water-mediated charged interactions with the sulfur dioxide moiety at 50% and 30% respectively Fig. 12.

Ligand Torsion analysis of **5u** showed that almost all bonds remained stable during the whole simulation, with relatively higher torsional behavior observed in bonds of bromofluorobenzene attachment with thiourea moiety Fig. 13.

The RMSF analysis of α-glucosidase showed that residues in the region of the active site lid in the protein structure showed the most flexibility during the simulation, with the highest value shown by *Phe 231* at 5.85 Å. Additionally, relatively higher fluctuations in the loop regions of the protein are expected due to the flexible nature of the loops. Overall, despite the conformation change of **5u**, the compound remained in the active site of the enzyme, and the complex **5u**-α-glucosidase observed to maintained stability throughout the simulation period of 150 ns.

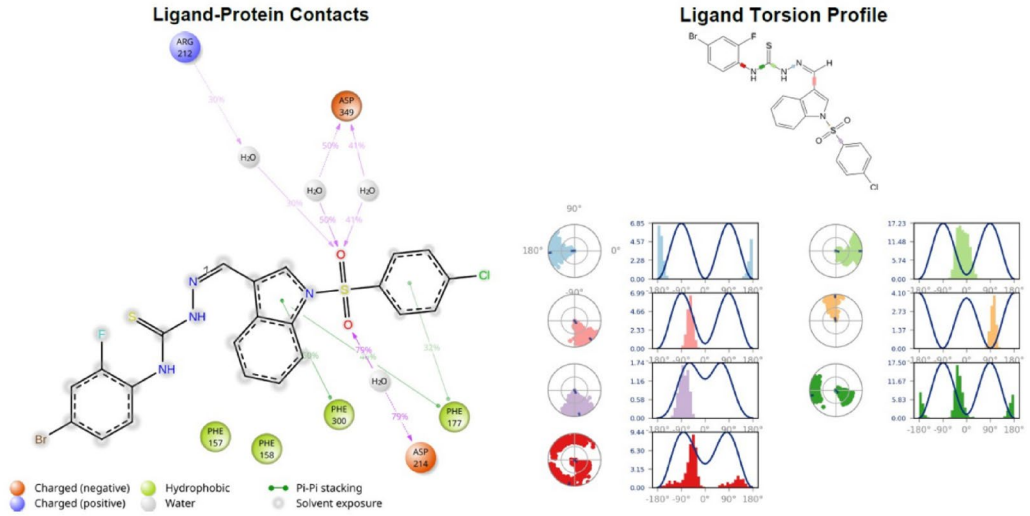

Fig. 13. Ligand-protein contacts and ligand-torsion profile of inhibitor **5u** with α-glucosidase during the simulation.

PCA PCA (principal component analysis), DCCM DCCM (dynamic cross-correlation matrix), and FEL (2.4.2. FEL (free energy landscape))

In PCA of protein Cα, the first two principal components capture 43% of protein movement during the simulation Fig. 14A. PC1 and PC2 account for 30.44% and 12.9% respectively. While the scatter plot shows clusters of frames with clear transitions of color, indicating the protein might have experienced substantial collective movement during the simulation, starting in one conformational basin and moving through different intermediate states before settling in a different basin. In Fig. 14B of binding site residues in 5 Å of **5u**, excluding ligand atoms, the first two principal components capture 47% of movement during the simulation. PC1 and PC2 account for 32.78% and 14.44% respectively. However, the scatter plot shows broadness without clustering of frames. Indicating the residues of the binding site alone could be flexible even without a ligand. This intrinsic dynamic nature of the binding site could be the reason for the ligand's changing conformations during the simulation.

In Fig. 14C of binding site residues in 5 Å of **5u**, including ligand atoms, the first two principal components capture about 68% of movement during the simulation. PC1 and PC2 account for 50.42% and 17.38% respectively. The scatter plot shows relatively compact clusters of frames. This is indicative of the coupled motion of the **5u** ligand with the binding site residues, suggesting the ligand **5u** could be producing the stabilizing effect to the specific conformations of the binding site or pocket, suggesting the ligand does not randomly drift; instead, the **5u**'s conformational shifts during the simulation could be part of the stable, collective movement in the binding pocket in the protein-ligand complex. In eigenvalue graphs of all three PCAs, the graphs show a comparatively sudden and sharp drop-off after the initial few components, suggesting that the majority of conformational changes are caused by the small number of large-amplitude, low-frequency movements.

While PCA shows overall collective movements, DCCM helps in understanding the coordinated movements and communication between the residues. In DCCM Fig. S53 heatmap of protein Cα, with sporadic weak to moderate correlations across the protein, all Cα atoms of residues, the connection between them seems mostly sparse. Indicating the expected behavior as the protein seems to undergo distributed movements in simulation, resulting in a lack of significant global correlated pattern, aligning with the overall flexibility of protein structures. In DCCM Fig. S54 heatmap of binding site residues in 5 Å of **5u**, excluding ligand atoms, fragmented local blocks of positive correlation along the diagonal can be observed. Indicating the somewhat coordinated movement of binding site residues, suggesting the flexibility of the binding site and pocket. However, in DCCM Fig. S55 heatmap of binding site residues in 5 Å of **5u**, including ligand atoms, the correlation blocks could be observed as relatively strong and well-defined, suggesting the correlation of the ligand **5u**'s atoms with the binding pocket residues. Indicating the coupling of ligand movement with the movement of the binding site. Suggesting that ligand **5u**, instead of drifting and random movement, integrates into the combined movement of the binding site. DCCM analysis shows that the ligand's RMSD fluctuations could be associated with the collective movement of the **5u**-coupled movement of the binding pocket.

RG-RMSD-based FEL showed a dominant deep basin located between 2.46 and 2.48 nm radius of gyration and 0.20–0.25 nm of RMSD. The basin is observed to be narrow, well-defined, with surrounding higher free energy regions. This suggests that the system converges into a dominant free energy minimum Fig. 15.

Overall, the post MD analyses indicate that despite the flexibility of the active/binding site, the **5u** ligand integrates into the movement of the site, resulting in the complex maintaining the stability during the simulation.

DFT studies

To strengthen the SAR rationale and provide mechanistic insight into the significant (up to 162-fold) improvement in α-glucosidase inhibition, quantum chemical calculations were performed for the eight most

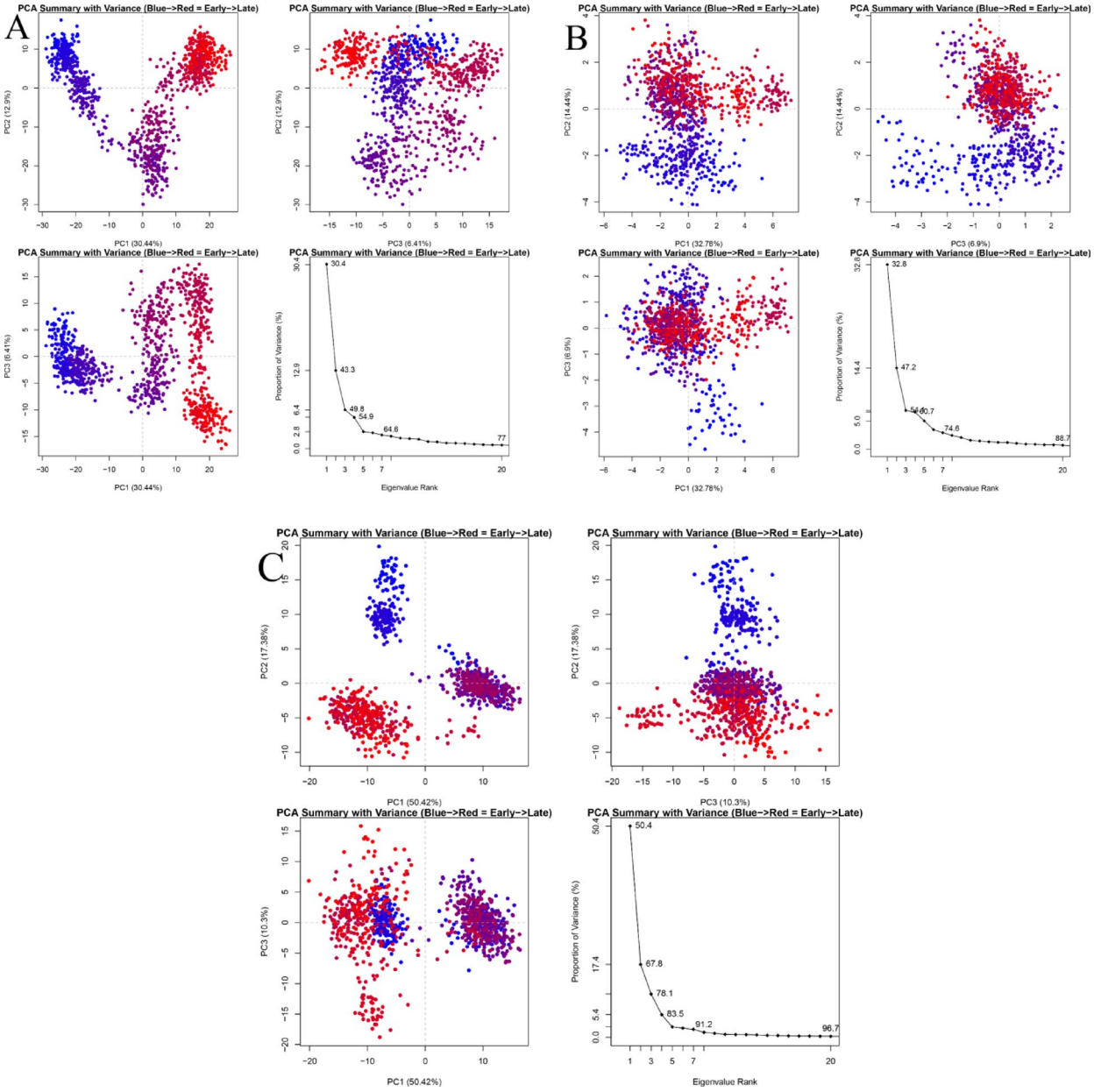

Fig. 14. [**A**] PCA summary of alpha carbon atoms of **5u**-alphaglucosidase complex; [**B**] PCA summary of binding site residues within 5 Å of **5u**, excluding **5u**'s atoms in **5u**-alphaglucosidase complex. [**C**] PCA summary of binding site residues within 5 angstroms of 5u, including 5u's atoms in 5u-alphaglucosidase complex.

active thiosemicarbazones **(5a**, **5 h**, **5 m**, **5n**, **5s**, **5t**, **5u**, **5w)** using the B3LYP/6-311 + + G(d, p)/GD3 level of theory. Geometry optimizations and vibrational analyses confirmed that all structures correspond to true minima on the potential energy surface as visualized in Fig. 16. The energetic parameters, such as optimization energies, dipole moments, and polarizabilities, are summarized in Table 3. Dipole moments (2.09–6.91 D) and polarizabilities (355–379 a.u.) suggested moderate molecular softness, favoring non-covalent interactions within the α-glucosidase binding pocket.

Frontier molecular orbitals and reactivity descriptors are computed, HOMO and LUMO energies ranged from − 6.00 to -5.85 eV and − 2.72 to -2.46 eV, respectively, with energy gaps (ΔƐ) between 3.14 and 3.48 eV. Smaller gaps (e.g., 3.14 eV for **5w**) indicate greater chemical reactivity and charge-transfer ability, aligning with their higher inhibitory potency (Fig. 17).

The global quantum chemical reactivity descriptors calculated for the eight most active thiosemicarbazone derivatives **(5a**, **5 h**, **5 m**, **5n**, **5s**, **5t**, **5u**, **5w)** provide insight into their electronic characteristics and potential interactions with α-glucosidase. Derived global reactivity descriptors (chemical potential μ, electronegativity χ, hardness η, softness ζ, and electrophilicity ω) are provided in Table 4.

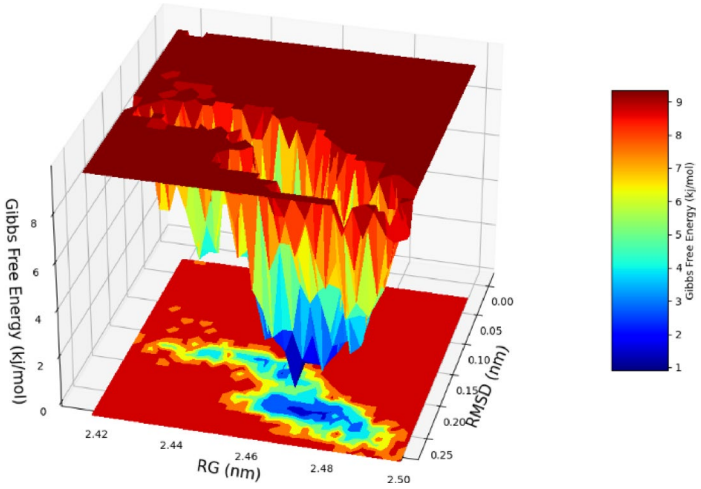

Fig. 15. Three-dimensional graph of free energy landscape analysis of 5u α-glucosidase simulation.

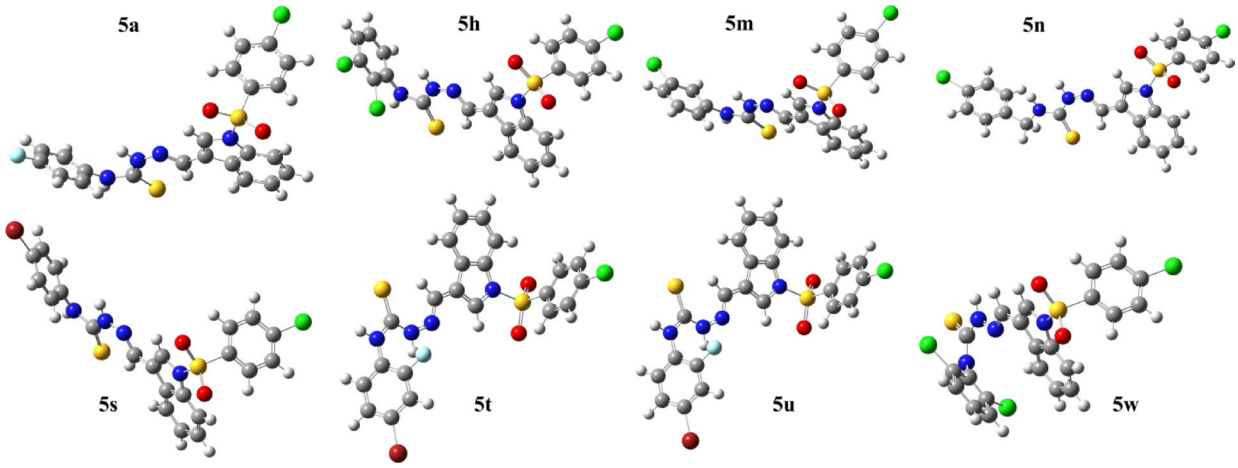

Fig. 16. Optimized structures of the investigated compounds at DFT/B3LYP/6-311G(d, p)/GD3 calculations in the gas phase.

Compound	Optimization energy (a.u.)	Dipole moment (Debye)	Polarizability (a.u.)	HOMO (eV)	LUMO (eV)	HOMO-LUMO (Δ eV)
Gas phase						
5a	-2573.6	3.71	355.3	-5.96	-2.49	3.46
5 h	-3393.6	6.72	370.5	-5.92	-2.47	3.45
5 m	-2934.0	2.09	371.6	-6.00	-2.52	3.48
5n	-2973.3	3.12	378.6	-5.89	-2.46	3.44
5s	-5047.8	3.68	378.0	-5.97	-2.50	3.47
5t	-2672.8	5.81	357.0	-5.92	-2.47	3.45
5u	-5147.1	3.92	374.5	-5.93	-2.47	3.46
5w	-3393.6	6.91	369.8	-5.85	-2.72	3.14

Table 3. Energetic parameters of top hits using DFT/B3LYP/6-311G(d, p)/GD3 in the S_0 gas phase.

The chemical potential **(μ)** values (-4.18 to -4.29 eV) highlights the tendency of these molecules to exchange electrons with their environment. More negative μ values (e.g., **5w**, -4.29 eV) indicate a greater propensity to donate electron density, favoring charge transfer to the electron-deficient regions of the enzyme's active site. Electronegativity **(χ)** values (4.18–4.29 eV) follow the same trend because χ = −μ. The close clustering of values suggests that all derivatives share similar electron-attracting ability, consistent with their narrow range of IC_{50} values relative to acarbose. Chemical hardness (η) values (1.57–1.74 eV) represent resistance to charge transfer.

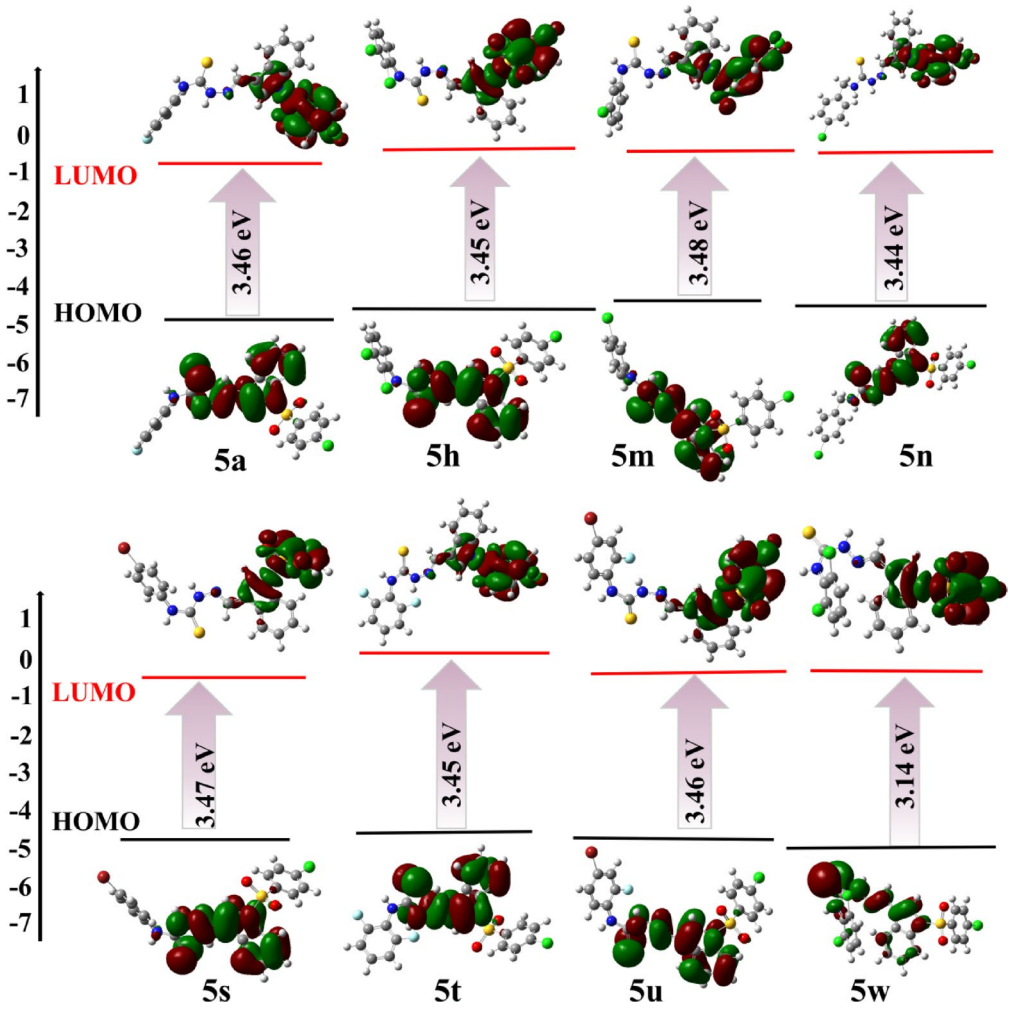

Fig. 17. HOMO-LUMO diagram of investigated compounds.

Compounds	Chemical potential μ (eV)	Electro-negativity χ (eV)	Chemical hardness η (eV)	Chemical softness ζ (eV)	Electrophilicity index ω (eV)	Ionization potential I (eV)	Electron affinity A (eV)
5a	-4.23	4.23	1.73	0.29	5.16	5.96	2.49
5 h	-4.19	4.19	1.73	0.29	5.09	5.92	2.47
5 m	-4.26	4.26	1.74	0.29	5.22	6.00	2.52
5n	-4.18	4.18	1.72	0.29	5.07	5.89	2.46
5s	-4.23	4.23	1.73	0.29	5.17	5.97	2.50
5t	-4.20	4.20	1.73	0.29	5.10	5.92	2.47
5u	-4.20	4.20	1.73	0.29	5.10	5.93	2.47
5w	-4.29	4.29	1.57	0.32	5.86	5.85	2.72

Table 4. The quantum chemical descriptors for top hits using DFT/B3LYP/6–311 g(d, p)/GD3 in the S_0 gas phase.

Lower η values correspond to greater chemical softness and enhanced polarizability. Compound **5w** exhibits the lowest hardness (1.57 eV) and, accordingly, the highest softness (ζ) (0.32 eV^{-1}), suggesting superior electronic adaptability during enzyme binding. The other potent inhibitors **(5a**, **5 h**, **5 m**, **5n**, **5s**, **5t**, **5u)** have slightly higher hardness (~ 1.72–1.74 eV), consistent with slightly less but still significant reactivity. This trend correlates with **5w's** competitive potency, as softer molecules can better stabilize non-covalent interactions and conform to the dynamic enzyme environment.

Electrophilicity indices (ω) (5.07–5.22 eV) quantify a molecule's capacity to accept electrons and support a tendency for strong electron acceptance, consistent with the enzyme's catalytic pocket being rich in nucleophilic

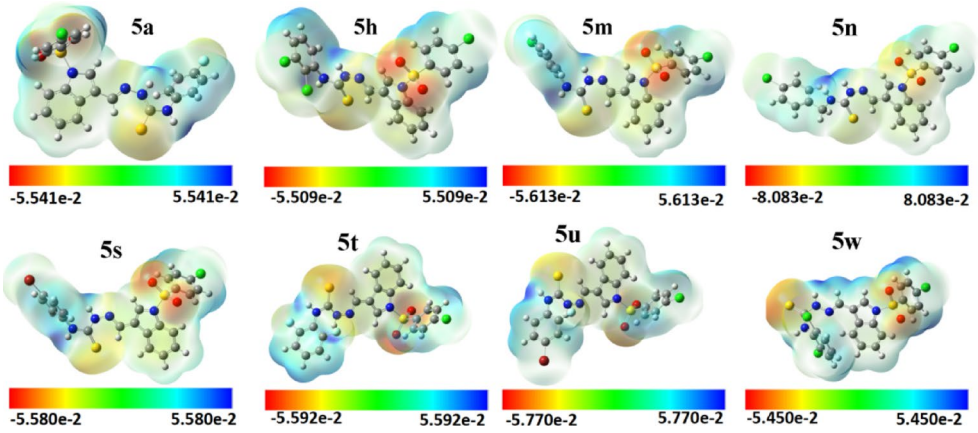

Fig. 18. Molecular electrostatic potential (MEP) maps for the investigated compounds at B3LYP/6–311 g(d, p)/GD3 level of theory in the gas phase.

residues. Higher ω values (e.g., 5 m, 5.22 eV; 5s, 5.17 eV) indicate stronger electrophilic character, which facilitates interactions with nucleophilic residues (e.g., Asp214, Asp349) in the α-glucosidase active site. This supports the docking results where these compounds showed extensive hydrogen bonding and π-cation/π-anion interactions.

The ionization potential **(I)** ranges in the window of 5.85-6.00 eV and electron affinities **(A)** (2.46–2.72 eV) indicate moderate stability against oxidation while maintaining sufficient ability to accept electrons. Compound **5w**, with the highest electron affinity (2.72 eV), is particularly suited to stabilize charge-transfer complexes within the catalytic pocket, possibly explaining its comparable potency to **5u** despite a slightly different R-group.

The combination of moderate hardness, high electrophilicity, and sizeable dipole moments for **5u**, **5 h**, **5w**, and **5s** suggests these molecules can effectively polarize and engage multiple types of interactions-electrostatic, hydrogen bonding, and π-stacking-within the enzyme binding site. By contrast, less active analogs (e.g., 5p from your biological data) likely have electronic properties less conducive to such multipoint binding. The descriptors therefore bridge steric considerations with a mechanistic electronic explanation: halogenated phenyl substituents modulate HOMO-LUMO gaps and electrostatic distributions to maximize enzyme-inhibitor affinity.

Molecular electrostatic potential (MEP) mapping surfaces (Fig. 18) highlight pronounced negative potential around the sulfonyl and thiocarbonyl groups and positive potential around the indole ring's NH group. These features correspond well with docking-identified hydrogen-bond donors/acceptors (Asp214, Asp349, Arg212) and hydrophobic contacts (Phe158, Phe300), reinforcing that electronic distribution, not only steric bulk, governs the binding mechanism.

Collectively, the DFT results corroborate the original steric/electronic SAR hypothesis that the indole-sulfonyl scaffold provides a rigid electron-withdrawing framework, while variations in R-group electronics subtly modulate HOMO-LUMO gaps, dipole moments, and electrostatic potentials. These electronic factors explain why halogenated phenyl substituents (e.g., **5u**, **5 h**, **5w**, **5s**) achieve superior inhibition compared to aliphatic or less polar groups, thereby providing a mechanistic justification for the observed activity enhancement. These descriptors correlate well with biological potency; **compound 5u** emerges as the most prominent inhibitor as it experimentally shows the lowest IC_{50} (5.38 μM) and 162-fold activity improvement over acarbose. Its dipole moment (3.92 D) and polarizability (374.5 a.u.) are among the highest values, suggesting strong electrostatic interactions and adaptability in the α-glucosidase pocket. **5u** showed the balanced HOMO–LUMO gap (ΔƐ = 3.46 eV), which maintains the reactivity without being unstable, indicating efficient charge transfer. Its electrophilicity index (5.10 eV) is high, meaning **5u** can accept electrons effectively, complementing nucleophilic residues in the catalytic triad. In docking studies, **5u** forms multiple hydrogen bonds and π-interactions with key residues (Asp214, Asp349, Arg212, Phe158), and MD simulations, hence showed that its complex remained stable throughout 150 ns. Although **5w** has the smallest hardness and slightly higher electron affinity, **5u** combines excellent electronic descriptors with the strongest experimental inhibition, making it the most prominent inhibitor overall.

Experimental

General

All the starting materials for the synthesis were purchased from Sigma-Aldrich Co. (Germany) and used without any purification. Solvents, including pure ethanol, methanol, DCM, etc., were obtained from various commercial suppliers and directly used in the reaction without purification. The reaction was monitored by thin-layer chromatography (TLC) on silica gel 60 aluminum plates, employing an appropriate solvent system. TLC spots were visualized under UV light at 254 nm. ^{1}H and ^{13}C NMR spectra were recorded on a Bruker 600 MHz / 400 MHz (151 MHz / 101 MHz) spectrometer using DMSO-d6 as the solvent. Coupling constants (*J*) were measured in Hertz (Hz), and chemical shifts were reported in parts per million (δ = ppm). Signal peaks were indicated as singlet (s), doublet (d), triplet (t), or multiplet (m). Melting points were determined with an MPS10 melting point apparatus. Mass spectra were obtained using a Bruker Daltonics mass spectrometer (ESI-MS).

General procedure for the synthesis of 1-((4-chlorophenyl)sulfonyl)-1*H*-indole-3-carbaldehyde (3)

Indole 3-carbaldehyde **(1)** (0.29 g, 2 mmol) was mixed with a solution of trimethylamine (0.36 mL, 2.6 mmol), DMAP (0.245 g, 2.0 mmol), and 4-chlorobenzenesulfonyl chloride **(2)** (0.4 g, 2 mmol) in DCM (15 mL) under argon atmosphere. At room temperature, the reaction mixture was stirred for 12 h. Upon completion of the reaction, a saturated solution of $NaHCO_3$ was added to the reaction mixture. The reaction mixture was extracted with dichloromethane. The combined organic layer was dried with Na_2SO_4, and the solvent was removed under vacuum. The residue was purified by flash chromatography (ethyl acetate/hexane 1/4). Solid precipitates of N-chlorophenyl sulfonyl indole-3-carbaldehyde **(3)** were obtained at the end of the reaction with an excellent yield of 92%.

General procedure for the synthesis of thiosemicarbazones 5(a-y)

To a solution of 1-((4-chlorophenyl)sulfonyl)-1*H*-indole-3-carbaldehyde **(3)** (0.1 g, 1 mmol) in 10 mL ethanol, equimolar quantities of substituted thiosemicarbazones **4(a-y)** (0.1 mmol) were added. Three to four drops of acetic acid were added as a catalyst. The reaction mixture was refluxed for 4–6 h until the completion of the reaction, as evidenced by TLC. Upon completion, the solid precipitates formed were washed with ethanol and filtered to obtain the thiosemicarbazones **5(a-y)**. The thiosemicarbazones were obtained with moderate to excellent yields.

Using spectrum analysis (^{13}C NMR and ^{1}H NMR), the structures of the newly synthesized compounds **5(a–y)** have been confirmed (Figs. S1–50).

2-({1-[(4-Chlorophenyl)sulfonyl]-1H-indol-3-yl}methylene)-N-(4-fluorophenyl)hydrazine-1-carbothioamide. (5a)
Color: White; Yield: 80%; m.p.: 232–233 °C; δ_H (400 MHz, DMSO-d_6) 11.91 (1 H, s), 9.80 (1 H, s), 8.46 (1 H, s), 8.40 (1 H, s), 8.31 (1 H, d, J = 7.8 Hz), 8.12–8.03 (2 H, m), 7.97 (1 H, d, J = 8.3 Hz), 7.76–7.65 (2 H, m), 7.61–7.52 (2 H, m), 7.45 (1 H, ddd, J = 8.4, 7.3, 1.3 Hz), 7.42–7.33 (1 H, m), 7.28–7.17 (2 H, m); ^{13}C NMR (101 MHz, DMSO) δ 176.73, 159.06 (d, $^{1}J_{F-C}$ = 248.4 Hz, 159.06 and 157.42,), 140.58, 138.51, 136.05, 135.08, 130.67, 130.34, 129.30, 128.74, 127.33, 126.47, 125.01, 123.60, 118.47, 115.38, 115.15, 113.53; m/z calculated for $C_{22}H_{16}ClFN_4O_2S_2$ ($[M+H]^+$) 487.0465, found 487.1418.

2-({1-[(4-Chlorophenyl)sulfonyl]-1H-indol-3-yl}methylene)-N-(4-methoxyphenyl)hydrazine-1-carbothioamide. (5b)
Color: White; Yield: 88%; m.p.: 215–216 °C; δ_H (600 MHz, DMSO-d_6) 11.81 (1 H, s), 9.69 (1 H, s), 8.45 (1 H, s), 8.38 (1 H, s), 8.30 (1 H, d, J = 7.9 Hz), 8.06 (2 H, d, J = 8.4 Hz), 7.97 (1 H, d, J = 8.3 Hz), 7.69 (2 H, d, J = 8.4 Hz), 7.51–7.30 (4 H, m), 6.94 (2 H, d, J = 8.5 Hz), 3.77 (3 H, s); ^{13}C NMR (151 MHz, DMSO) δ 176.72, 157.52, 140.57, 138.06, 135.78, 135.08, 132.56, 130.66, 130.13, 129.28, 128.11, 127.36, 126.42, 124.98, 123.55, 118.52, 113.82, 113.48, 55.73; m/z calculated for $C_{23}H_{19}ClN_4O_3S_2$ ($[M+H]^+$) 499.0665, found 499.0589.

N-Benzyl-2-({1-[(4-Chlorophenyl)sulfonyl]-1H-indol-3-yl}methylene)hydrazine-1-carbothioamide. (5c)
Color: White; Yield: 86%; m.p.: 206–207 °C; δ_H (600 MHz, DMSO-d_6) 11.68 (1 H, s), 8.64 (1 H, t, J = 6.3 Hz), 8.37 (1 H, s), 8.34 (1 H, s), 8.28 (1 H, d, J = 7.9 Hz), 8.09–8.01 (2 H, m), 7.96 (1 H, d, J = 8.4 Hz), 7.68 (2 H, d, J = 8.7 Hz), 7.44 (1 H, t, J = 7.6 Hz), 7.40–7.29 (5 H, m), 7.29–7.21 (1 H, m), 4.90 (2 H, d, J = 6.2 Hz); ^{13}C NMR (151 MHz, DMSO) δ 177.86, 140.56, 139.86, 138.10, 135.77, 135.11, 130.64, 130.30, 129.28, 128.68, 127.46, 127.21, 127.17, 126.44, 124.95, 123.68, 118.54, 113.48, 47.23. m/z calculated for $C_{23}H_{19}ClN_4O_2S_2$ $[M+H]^+$ 483.0716, found 483.0943.

2-({1-[(4-Chlorophenyl)sulfonyl]-1H-indol-3-yl}methylene)-N-(4-nitrophenyl)hydrazine-1-carbothioamide. (5d)
Color: Light yellowish; Yield: 60%; m.p.: 231–232 °C; δ_H (400 MHz, DMSO-d_6) 12.26 (1 H, s), 10.23 (1 H, s), 8.49 (1 H, s), 8.44 (1 H, s), 8.31–8.20 (3 H, m), 8.14–8.02 (4 H, m), 7.98 (1 H, d, J = 8.2 Hz), 7.76–7.65 (2 H, m), 7.46 (1 H, ddd, J = 8.4, 7.2, 1.4 Hz), 7.43–7.34 (1 H, m); ^{13}C NMR (101 MHz, DMSO) δ 175.67, 146.07, 143.81, 140.63, 139.63, 135.74, 135.11, 130.96, 130.67, 129.31, 127.24, 126.51, 125.04, 124.50, 124.35, 123.58, 118.28, 113.53; m/z calculated for $C_{22}H_{16}ClN_5O_4S_2$ ($[M+H]^+$) 514.0410, found 514.0335.

2-({1-[(4-Chlorophenyl)sulfonyl]-1H-indol-3-yl}methylene)-N-methylhydrazine-1-carbothioamide. (5e)
Color: White; Yield: 66%; m.p.: 256–257 °C; δ_H (600 MHz, DMSO-d_6) 11.53 (1 H, s), 8.33 (2 H, d, J = 11.3 Hz), 8.29 (1 H, s), 8.11 (1 H, q, J = 4.5 Hz), 8.08–8.04 (2 H, m), 7.96 (1 H, d, J = 8.3 Hz), 7.71–7.64 (2 H, m), 7.49–7.42 (1 H, m), 7.38 (1 H, t, J = 7.6 Hz), 3.36 (5 H, s); ^{13}C NMR (151 MHz, DMSO) δ 177.98, 140.55, 137.64, 135.80, 135.10, 130.64, 130.12, 129.28, 127.19, 126.43, 124.97, 123.86, 118.61, 113.42, 31.67; m/z calculated for $C_{17}H_{15}ClN_4O_2S_2$ ($[M+H]^+$) 407.0403, found 407.0327.

2-({1-[(4-Chlorophenyl)sulfonyl]-1H-indol-3-yl}methylene)-N-phenylhydrazine-1-carbothioamide. (5f)
Color: White; Yield: 71%; m.p.: 224–225 °C; δ_H (600 MHz, DMSO-d_6) 11.89 (1 H, s), 9.80 (1 H, s), 8.46 (1 H, s), 8.40 (1 H, s), 8.29 (1 H, d, J = 7.9 Hz), 8.07 (2 H, d, J = 8.5 Hz), 7.97 (1 H, d, J = 8.4 Hz), 7.70 (2 H, d, J = 8.4 Hz), 7.59 (2 H, d, J = 7.8 Hz), 7.45 (1 H, t, J = 7.8 Hz), 7.38 (3 H, td, J = 7.5, 4.6 Hz), 7.22 (1 H, t, J = 7.4 Hz); ^{13}C NMR (151 MHz, DMSO) δ 176.29, 140.59, 139.66, 138.34, 135.78, 135.09, 130.67, 130.33, 129.29, 128.63, 127.34, 126.44, 126.23, 125.82, 125.01, 123.53, 118.47, 113.50; m/z calculated for $C_{22}H_{17}ClN_4O_2S_2$ ($[M+H]^+$) 469.0559, found 469.0485.

2-({1-[(4-Chlorophenyl)sulfonyl]-1H-indol-3-yl}methylene)-N-cyclohexylhydrazine-1-carbothioamide. (5 g)
Color: White shinny; Yield: 70%; m.p.: 222–223 °C; δ_H (600 MHz, DMSO-d_6) 11.56 (1 H, s), 8.37 (1 H, s), 8.29 (1 H, s), 8.10 (1 H, d, J = 7.9 Hz), 8.08–8.01 (2 H, m), 7.98 (1 H, d, J = 8.3 Hz), 7.71–7.66 (2 H, m), 7.64 (1 H, d, J = 8.4 Hz), 7.48–7.43 (1 H, m), 7.40 (1 H, t, J = 7.6 Hz), 4.17 (1 H, qd, J = 10.2, 4.4 Hz), 1.92 (2 H, dq, J = 12.5, 4.1 Hz), 1.70 (2 H, dt, J = 13.3, 4.0 Hz), 1.57 (1 H, dt, J = 12.9, 4.1 Hz), 1.51–1.39 (2 H, m), 1.41–1.28 (2 H, m), 1.28–1.15 (1 H, m); ^{13}C NMR (151 MHz, DMSO) δ 176.07, 140.56, 137.59, 135.76, 135.17, 130.63, 130.25, 129.29, 127.28, 126.46, 125.06, 122.98, 118.52, 113.71, 52.55, 32.16, 25.53, 24.96; m/z calculated for ([M + H]$^+$) $C_{22}H_{23}ClN_4O_2S_2$ 475.1029, found 475.0953.

2-({1-[(4-Chlorophenyl)sulfonyl]-1H-indol-3-yl}methylene)-N-(2,3-dichlorophenyl)hydrazine-1-carbothioamide. (5 h)
Color: White; Yield: 84%; m.p.: 244–245 °C; δ_H (600 MHz, DMSO-d_6) 12.16 (1 H, s), 9.79 (1 H, s), 8.46 (1 H, s), 8.42 (1 H, s), 8.39 (1 H, d, J = 7.9 Hz), 8.08 (2 H, d, J = 8.3 Hz), 7.97 (1 H, d, J = 8.4 Hz), 7.84 (1 H, d, J = 8.1 Hz), 7.70 (2 H, d, J = 8.3 Hz), 7.57 (1 H, d, J = 8.1 Hz), 7.44 (2 H, dt, J = 20.9, 7.9 Hz), 7.36 (1 H, t, J = 7.6 Hz); ^{13}C NMR (151 MHz, DMSO) δ 176.43, 140.63, 139.34, 139.02, 135.77, 135.11, 132.06, 131.18, 130.68, 129.32, 128.68, 128.46, 128.02, 127.06, 126.53, 124.97, 123.79, 118.23, 113.50; m/z calculated for $C_{22}H_{15}Cl_3N_4O_2S_2$ ([M + H]$^+$) 536.9780, found 537.1505.

2-({1-[(4-Chlorophenyl)sulfonyl]-1H-indol-3-yl}methylene)-N-(2,6-dimethylphenyl)hydrazine-1-carbothioamide. (5i)
Color: White; Yield: 77%; m.p.: 245–246 °C; δ_H (600 MHz, DMSO-d_6) 11.78 (1 H, s), 9.46 (1 H, s), 8.47–8.40 (2 H, m), 8.39 (1 H, s), 8.12–8.02 (2 H, m), 7.95 (1 H, d, J = 8.3 Hz), 7.75–7.66 (2 H, m), 7.44 (1 H, t, J = 7.8 Hz), 7.33 (1 H, t, J = 7.6 Hz), 7.12 (3 H, q, J = 5.6 Hz), 2.21 (6 H, s); ^{13}C NMR (151 MHz, DMSO) δ 176.98, 140.55, 138.10, 137.88, 137.07, 135.80, 135.09, 130.64, 130.31, 129.26, 128.06, 127.39, 127.27, 126.40, 124.93, 124.06, 118.65, 113.35, 18.55; m/z calculated for $C_{24}H_{21}ClN_4O_2S_2$ ([M + H]$^+$) 497.0872, found 497.0795.

2-({1-[(4-Chlorophenyl)sulfonyl]-1H-indol-3-yl}methylene)-N-(4-methylbenzyl)hydrazine-1-carbothioamide. (5j)
Color: Off white; Yield: 70%; m.p.: 205–206 °C; δ_H (600 MHz, DMSO-d_6) 11.65 (1 H, s), 8.58 (1 H, t, J = 6.2 Hz), 8.37 (1 H, s), 8.33 (1 H, s), 8.26 (1 H, d, J = 7.9 Hz), 8.05 (2 H, d, J = 8.7 Hz), 7.96 (1 H, d, J = 8.4 Hz), 7.68 (2 H, d, J = 8.7 Hz), 7.48–7.39 (1 H, m), 7.33 (1 H, t, J = 7.6 Hz), 7.24 (2 H, d, J = 7.7 Hz), 7.13 (2 H, d, J = 7.8 Hz), 4.85 (2 H, d, J = 6.1 Hz), 2.27 (3 H, s); ^{13}C NMR (151 MHz, DMSO) δ 177.74, 140.56, 138.01, 136.77, 136.22, 135.77, 135.11, 130.64, 130.26, 129.28, 129.22, 127.49, 127.21, 126.43, 124.94, 123.64, 118.54, 113.48, 46.99, 21.15; m/z calculated for $C_{24}H_{21}ClN_4O_2S_2$ ([M + H]$^+$) 497.0872, found 497.0795.

2-({1-[(4-Chlorophenyl)sulfonyl]-1H-indol-3-yl}methylene)-N-(3-methoxyphenyl)hydrazine-1-carbothioamide. (5k)
Color: White; Yield: 50%; m.p.: 221–222 °C; δ_H (600 MHz, DMSO-d_6) 11.90 (1 H, s), 9.77 (1 H, s), 8.46 (1 H, s), 8.39 (1 H, s), 8.27 (1 H, d, J = 7.9 Hz), 8.11–8.04 (2 H, m), 7.97 (1 H, d, J = 8.3 Hz), 7.74–7.67 (2 H, m), 7.48–7.41 (1 H, m), 7.38 (1 H, t, J = 7.6 Hz), 7.34–7.23 (2 H, m), 7.20–7.14 (1 H, m), 6.79 (1 H, dd, J = 8.2, 2.5 Hz), 3.77 (3 H, s); ^{13}C NMR (151 MHz, DMSO) δ 176.02, 159.55, 140.74, 140.59, 138.36, 135.77, 135.10, 130.67, 130.37, 129.36, 129.30, 127.33, 126.45, 125.02, 123.48, 118.46, 118.08, 113.53, 111.58, 111.21, 55.63; m/z calculated for $C_{23}H_{19}ClN_4O_3S_2$ ([M + H]$^+$) 499.0665, found 499.0589.

2-({1-[(4-Chlorophenyl)sulfonyl]-1H-indol-3-yl}methylene)-N-(3-nitrophenyl)hydrazine-1-carbothioamide. (5 L)
Color: White; Yield: 83%; m.p.: 230–231 °C; δ_H (600 MHz, DMSO-d_6) 12.15 (1 H, s), 10.13 (1 H, s), 8.66 (1 H, t, J = 2.2 Hz), 8.48 (1 H, s), 8.43 (1 H, s), 8.32 (1 H, d, J = 7.9 Hz), 8.06 (4 H, td, J = 8.5, 2.3 Hz), 7.97 (1 H, d, J = 8.3 Hz), 7.70 (2 H, d, J = 8.7 Hz), 7.66 (1 H, t, J = 8.2 Hz), 7.46 (1 H, t, J = 7.6 Hz), 7.38 (1 H, t, J = 7.6 Hz); ^{13}C NMR (151 MHz, DMSO) δ 176.30, 147.80, 140.98, 140.62, 139.40, 135.75, 135.10, 132.43, 130.76, 130.67, 129.78, 129.31, 127.28, 126.49, 125.02, 123.68, 120.16, 118.34, 113.50; m/z calculated for $C_{22}H_{16}ClN_5O_4S_2$ ([M + H]$^+$) 514.0410, found 514.0335.

N-(3-Chlorophenyl)-2-({1-[(4-chlorophenyl)sulfonyl]-1H-indol-3-yl}methylene)hydrazine-1-carbothioamide. (5 m)
Color: White; Yield: 83%; m.p.: 216–217 °C; δ_H (600 MHz, DMSO-d_6) 12.02 (1 H, s), 9.89 (1 H, s), 8.47 (1 H, s), 8.41 (1 H, s), 8.29 (1 H, d, J = 7.9 Hz), 8.11–8.03 (2 H, m), 7.97 (1 H, d, J = 8.3 Hz), 7.79 (1 H, t, J = 2.1 Hz), 7.70 (2 H, d, J = 8.7 Hz), 7.60–7.53 (1 H, m), 7.49–7.43 (1 H, m), 7.39 (2 H, dt, J = 12.8, 7.8 Hz), 7.31–7.23 (1 H, m); ^{13}C NMR (151 MHz, DMSO) δ 176.20, 141.20, 140.60, 138.89, 135.76, 135.09, 132.69, 130.66, 130.54, 130.15, 129.30, 127.30, 126.46, 125.64, 125.49, 125.01, 124.77, 123.60, 118.38, 113.49; m/z calculated for $C_{22}H_{16}Cl_2N_4O_2S_2$ ([M + H]$^+$) 503.0170, found 503.0095.

N-(4-Chlorobenzyl)-2-({1-[(4-chlorophenyl)sulfonyl]-1H-indol-3-yl}methylene)hydrazine-1-carbothioamide. (5n)
Color: White shinny; Yield: 82%; m.p.: 214–215 °C; δ_H (600 MHz, DMSO-d_6) 11.69 (1 H, s), 8.69 (1 H, t, J = 6.2 Hz), 8.37 (1 H, s), 8.34 (1 H, s), 8.30 (1 H, d, J = 7.9 Hz), 8.09–8.02 (2 H, m), 7.96 (1 H, d, J = 8.4 Hz), 7.72–7.64 (2 H, m), 7.48–7.42 (1 H, m), 7.42–7.33 (5 H, m), 4.88 (2 H, d, J = 6.2 Hz); ^{13}C NMR (151 MHz, DMSO) δ 177.91, 140.57, 139.00, 138.30, 135.77, 135.10, 131.66, 130.64, 130.35, 129.36, 129.28, 128.59, 127.19, 126.44, 124.97, 123.74, 118.51, 113.46, 46.59; m/z calculated for $C_{23}H_{18}Cl_2N_4O_2S_2$ ([M + H]$^+$) 517.0326, found 517.0250.

2-({1-[(4-Chlorophenyl)sulfonyl]-1H-indol-3-yl}methylene)-N-phenethylhydrazine-1-carbothioamide. (5o)
Color: White; Yield: 60%; m.p.: 227–228 °C; δ_H (600 MHz, DMSO-d_6) 11.59 (1 H, s), 8.34 (1 H, s), 8.28 (1 H, s), 8.10 (1 H, d, J = 7.9 Hz), 7.96 (1 H, d, J = 8.4 Hz), 7.72–7.66 (2 H, m), 7.46 (1 H, ddd, J = 8.4, 7.3, 1.3 Hz), 7.39–7.33 (1 H, m), 7.34–7.28 (4 H, m), 7.22 (1 H, td, J = 6.1, 2.8 Hz), 3.85 (2 H, dt, J = 8.2, 6.2 Hz), 2.95 (2 H, t, J = 7.5 Hz); ^{13}C NMR (151 MHz, DMSO) δ 177.17, 140.57, 139.67, 137.96, 135.77, 135.12, 130.65, 130.41, 129.30, 129.06, 128.93, 127.13, 126.69, 126.45, 125.02, 123.56, 118.50, 113.49, 45.41, 35.16; m/z calculated for $C_{24}H_{21}ClN_4O_2S_2$ ($[M+H]^+$) 497.0872, found 497.0796.

2-({1-[(4-Chlorophenyl)sulfonyl]-1H-indol-3-yl}methylene)-N-isobutylhydrazine-1-carbothioamide. (5p)
Color: White; Yield: 80%; m.p.: 239–240 °C; δ_H (600 MHz, DMSO-d_6) 11.54 (1 H, s), 8.36 (1 H, s), 8.30 (1 H, s), 8.24 (1 H, d, J = 7.9 Hz), 8.10–8.03 (3 H, m), 7.97 (1 H, d, J = 8.4 Hz), 7.71–7.65 (2 H, m), 7.45 (1 H, ddd, J = 8.4, 7.2, 1.3 Hz), 7.41–7.33 (1 H, m), 3.46 (2 H, t, J = 6.5 Hz), 2.01 (1 H, hept, J = 6.8 Hz), 0.91 (6 H, d, J = 6.7 Hz); ^{13}C NMR (151 MHz, DMSO) δ 177.49, 140.55, 137.63, 135.77, 135.16, 130.63, 130.26, 129.28, 127.25, 126.45, 124.95, 123.46, 118.61, 113.58, 51.18, 28.31, 20.43; m/z calculated for $C_{20}H_{21}ClN_4O_2S_2$ ($[M+H]^+$) 449.0872, found 449.0795.

2-({1-[(4-Chlorophenyl)sulfonyl]-1H-indol-3-yl}methylene)-N-(3-(methylthio)propyl)hydrazine-1-carbothioamide. (5q)
Color: White; Yield: 68%; m.p.: 172–173 °C; δ_H (600 MHz, DMSO-d_6) 11.53 (1 H, s), 8.35 (1 H, s), 8.28 (2 H, d, J = 13.1 Hz), 8.18 (1 H, t, J = 6.0 Hz), 8.09–8.02 (2 H, m), 7.96 (1 H, d, J = 8.3 Hz), 7.73–7.65 (2 H, m), 7.45 (1 H, ddd, J = 8.4, 7.3, 1.3 Hz), 7.42–7.35 (1 H, m), 3.69 (2 H, q, J = 6.7 Hz), 2.56–2.49 (3 H, m), 2.06 (3 H, s), 1.90 (2 H, p, J = 7.2 Hz); ^{13}C NMR (151 MHz, DMSO) δ 177.29, 140.56, 137.79, 135.78, 135.12, 130.64, 130.21, 129.29, 127.22, 126.45, 124.96, 123.65, 118.58, 113.50, 43.31, 31.25, 28.68, 15.16; m/z calculated for $C_{20}H_{21}ClN_4O_2S_3$ ($[M+H]^+$) 481.0593, found 481.0517.

2-({1-[(4-Chlorophenyl)sulfonyl]-1H-indol-3-yl}methylene)-N-(2-(trifluoromethyl)phenyl)hydrazine-1-carbothioamide. (5r)
Color: White; Yield: 83%; m.p.: 236–237 °C; δ_H (600 MHz, DMSO-d_6) 12.14 (1 H, s), 9.58 (1 H, s), 8.45 (1 H, s), 8.42 (1 H, s), 8.31 (1 H, d, J = 7.9 Hz), 8.12–8.04 (2 H, m), 7.97 (1 H, d, J = 8.4 Hz), 7.80–7.75 (2 H, m), 7.73 (1 H, td, J = 7.7, 1.5 Hz), 7.71–7.67 (2 H, m), 7.52 (1 H, t, J = 7.6 Hz), 7.44 (1 H, ddd, J = 8.3, 7.2, 1.2 Hz), 7.36–7.29 (1 H, m); ^{13}C NMR (151 MHz, DMSO) δ 177.22, 140.63, 139.18, 137.68, 135.77, 135.13, 132.88, 132.34, 131.25, 130.67, 129.32, 127.55, 127.03, 126.49 (q, $^3J_{F-C}$ = 4.8 Hz, 126.52 126.50, 126.46, 126.43), 126.52, 126.49, 126.46, 126.01, 125.82, 125.07, 124.90, 123.67, 123.26, 118.25, 113.49; m/z calculated for $C_{23}H_{16}ClF_3N_4O_2S_2$ ($[M+H]^+$) 537.0433, found 537.0358.

N-(4-Bromophenyl)-2-({1-[(4-chlorophenyl)sulfonyl]-1H-indol-3-yl}methylene)hydrazine-1-carbothioamide. (5s)
Color: White; Yield: 70%; m.p.: 236–237 °C; δ_H (600 MHz, DMSO-d_6) 11.97 (1 H, s), 9.84 (1 H, s), 8.46 (1 H, s), 8.40 (1 H, s), 8.28 (1 H, d, J = 7.9 Hz), 8.10–8.05 (2 H, m), 7.97 (1 H, d, J = 8.3 Hz), 7.72–7.67 (2 H, m), 7.61–7.53 (4 H, m), 7.45 (1 H, ddd, J = 8.4, 7.2, 1.3 Hz), 7.40–7.34 (1 H, m); ^{13}C NMR (151 MHz, DMSO) δ 176.23, 140.60, 139.12, 138.73, 135.77, 135.08, 131.43, 130.67, 130.46, 129.30, 128.21, 127.30, 126.46, 125.00, 123.58, 118.41, 118.03, 113.49; m/z calculated for $C_{22}H_{16}BrClN_4O_2S_2$ ($[M+H]^+$) 546.9664, found 546.9588.

2-({1-[(4-Chlorophenyl)sulfonyl]-1H-indol-3-yl}methylene)-N-(2,6-difluorophenyl)hydrazine-1-carbothioamide. (5t)
Color: White; Yield: 75%; m.p.: 232–233 °C; δ_H (600 MHz, DMSO-d_6) 12.13 (1 H, s), 9.39 (1 H, s), 8.46 (1 H, s), 8.41 (2 H, d, J = 10.4 Hz), 8.12–8.05 (2 H, m), 7.96 (1 H, d, J = 8.4 Hz), 7.74–7.67 (2 H, m), 7.45 (2 H, tdd, J = 6.5, 5.2, 1.7 Hz), 7.38–7.32 (1 H, m), 7.20 (2 H, t, J = 8.0 Hz); ^{13}C NMR (151 MHz, DMSO) δ 178.16, 160.43 (d, $^1J_{F-C}$ = 244.5 Hz, 160.43 and 158.81), 140.61, 139.41, 135.77, 135.06, 130.82, 130.68, 129.48, 129.31, 127.13, 126.48, 124.95, 123.97, 118.26, 117.62, 113.38, 112.26, 112.23, 112.11; m/z calculated for $C_{22}H_{15}ClF_2N_4O_2S_2$ ($[M+H]^+$) 505.037, found 505.0295.

N-(4-Bromo-2-fluorophenyl)-2-({1-[(4-chlorophenyl)sulfonyl]-1H-indol-3-yl}methylene)hydrazine-1-carbothioamide. (5u)
Color: White; Yield: 80%; m.p.: 225–226 °C; δ_H (600 MHz, DMSO-d_6) 12.13 (1 H, s), 9.62 (1 H, s), 8.46 (1 H, s), 8.41 (1 H, s), 8.33 (1 H, d, J = 7.9 Hz), 8.11–8.04 (2 H, m), 7.97 (1 H, d, J = 8.4 Hz), 7.73–7.67 (3 H, m), 7.65 (1 H, dd, J = 9.7, 2.2 Hz), 7.50–7.41 (2 H, m), 7.36 (1 H, t, J = 7.5 Hz); ^{13}C NMR (151 MHz, DMSO) δ 176.92, 158.18 (d, $^1J_{F-C}$ = 251.4 Hz, 158.18 and 156.51), 140.62, 139.24, 135.76, 135.10, 131.32, 130.94, 130.68, 129.31, 127.64, 127.61, 127.59, 127.52, 127.12, 126.50, 124.97, 123.69, 119.56, 119.40, 119.24, 119.18, 118.24, 113.48; m/z calculated for $C_{22}H_{15}BrClFN_4O_2S_2$ ($[M+H]^+$) 564.9570, found 564.9495.

2-({1-[(4-Chlorophenyl)sulfonyl]-1H-indol-3-yl}methylene)hydrazine-1-carbothioamide. (5v)
Color: White; Yield: 80%; m.p.: 238–239 °C; δ_H (600 MHz, DMSO-d_6) 11.50 (1 H, s), 8.35 (1 H, s), 8.34–8.24 (3 H, m), 8.08–8.02 (2 H, m), 7.95 (1 H, d, J = 8.4 Hz), 7.70–7.62 (3 H, m), 7.44 (1 H, ddd, J = 8.5, 7.3, 1.3 Hz), 7.38–7.32 (1 H, m);^{13}C NMR (151 MHz, DMSO) δ 178.05, 140.55, 138.12, 135.79, 135.10, 130.63, 130.41, 129.27, 127.16, 126.41, 125.04, 123.96, 118.57, 113.40; m/z calculated for $C_{16}H_{13}ClN_4O_2S_2$ ($[M+H]^+$) 393.0246, found 393.0170.

2-({1-[(4-Chlorophenyl)sulfonyl]-1H-indol-3-yl}methylene)-N-(2,6-dichlorophenyl)hydrazine-1-carbothioamide. (5w)
Color: White; Yield: 70%; m.p.: 225–226 °C; δ_H (600 MHz, DMSO-d_6) 12.04 (1 H, s), 9.66 (1 H, s), 8.43 (2 H, d, *J* = 7.0 Hz), 8.40 (1 H, s), 8.10–8.04 (2 H, m), 7.96 (1 H, d, *J* = 8.4 Hz), 7.73–7.67 (2 H, m), 7.56 (2 H, d, *J* = 8.1 Hz), 7.45 (1 H, ddd, *J* = 8.4, 7.2, 1.3 Hz), 7.39 (1 H, t, *J* = 8.1 Hz), 7.37–7.32 (1 H, m); ^{3}C NMR (151 MHz, DMSO) δ 177.30, 140.59, 138.96, 135.84, 135.78, 135.08, 130.72, 130.67, 129.82, 129.29, 128.76, 127.17, 126.47, 124.95, 124.11, 118.40, 113.36; m/z calculated for $C_{22}H_{15}Cl_3N_4O_2S_2$ ($[M+H]^+$) 536.9780, found 536.9705.

2-({1-[(4-Chlorophenyl)sulfonyl]-1H-indol-3-yl}methylene)-N-(2,4-dimethylphenyl)hydrazine-1-carbothioamide. (5x)
Color: White; Yield: 79%; m.p.: 236–237 °C; δ_H (600 MHz, DMSO-d_6) 11.80 (1 H, s), 9.51 (1 H, s), 8.43 (1 H, s), 8.38 (1 H, s), 8.36 (1 H, d, *J* = 7.9 Hz), 8.09–8.03 (2 H, m), 7.96 (1 H, d, *J* = 8.3 Hz), 7.73–7.66 (2 H, m), 7.44 (1 H, ddd, *J* = 8.4, 7.2, 1.2 Hz), 7.38–7.31 (1 H, m), 7.23 (1 H, d, *J* = 7.9 Hz), 7.11–7.06 (1 H, m), 7.03 (1 H, dd, *J* = 8.1, 2.1 Hz), 2.29 (3 H, s), 2.21 (3 H, s); ^{13}C NMR (151 MHz, DMSO) δ 177.04, 140.57, 138.08, 136.23, 136.04, 135.80, 135.39, 135.08, 131.07, 130.66, 130.29, 129.28, 128.92, 127.27, 126.88, 126.42, 124.92, 123.77, 118.55, 113.43, 21.08, 18.21; m/z calculated for $C_{24}H_{21}ClN_4O_2S_2$ ($[M+H]^+$) 497.0872, found 497.0795.

2-({1-[(4-Chlorophenyl)sulfonyl]-1H-indol-3-yl}methylene)-N-(naphthalen-1-yl)hydrazine-1-carbothioamide. (5y)
Color: White; Yield: 80%; m.p.: 234–235 °C; δ_H (600 MHz, DMSO-d_6) 11.99 (1 H, s), 10.05 (1 H, s), 8.48 (2 H, d, *J* = 6.3 Hz), 8.41 (1 H, d, *J* = 8.0 Hz), 8.12–8.04 (2 H, m), 8.02–7.95 (2 H, m), 7.91 (2 H, ddd, *J* = 9.4, 5.9, 2.8 Hz), 7.73–7.67 (2 H, m), 7.62–7.50 (4 H, m), 7.43 (1 H, ddd, *J* = 8.4, 7.2, 1.2 Hz), 7.31 (1 H, t, *J* = 7.5 Hz); ^{13}C NMR (151 MHz, DMSO) δ 178.01, 140.59, 138.43, 136.23, 135.80, 135.10, 134.20, 131.08, 130.67, 130.39, 129.29, 128.53, 127.40, 127.31, 126.91, 126.63, 126.51, 126.43, 125.93, 124.91, 123.82, 123.67, 118.56, 113.43; m/z calculated for $C_{26}H_{19}ClN_4O_2S_2$ ($[M+H]^+$) 519.0716, found 519.0639.

In-silico studies

Molecular docking studies were carried out using BioSolveIT's LeadIT software (v 3.2.1; BioSolveIT GmbH, 2024). Visualization of docked conformations and interactions with binding site amino acids was performed using BIOVIA Discovery Studio Visualizer (v 4.5; BIOVIA, Dassault Systèmes, 2019). The crystal structure of S. cerevisiae α-glucosidase is not available from the PDB; hence its homology model was built and validated according to our already reported method. The most active inhibitors **5u**, **5w**, and **5 h** were selected. A total of 10 docked conformations were generated for each inhibitor; finally, the conformation having the most favorable docking score was selected for further evaluation. The MD simulation study of inhibitor **5u**-α-Glucosidase complex was performed on the Desmond Module (D.E. Shaw) in Schrödinger Maestro 2024.4 for 150 ns[52]. The complex of inhibitor 5u with α-glucosidase was used. Protein Preparation was used for pre-processing, refinement, and Capping of the termini of the protein structure, and then the hydrogen bond assignment was optimized. Solvation was carried out through the system builder panel by a pre-defined TIP3P solvent model, an orthorhombic box shape was used with buffer dimensions of 10 Å x 10 Å x 10 Å and minimized volume. Ions placement for neutralization was used as the provided default calculated by software, and 0.15 M NaCl salt was also added to simulate the biological natural environments[53]. In the Molecular Dynamics panel, 150 ns (nanoseconds) time of simulation was entered. In contrast, the trajectory of the simulation was set to be recorded after every 150 ps (picoseconds) which resulted in approximately 1000 frames. The system was run using the default relaxation protocol, NPT ensemble at 300 K temperature and 1.01325 bar pressure using Nosé-Hoover chain thermostat, and Martyna-Tobias-Klein barostat settings were used for the production run of 150ns simulation for the complex. The analysis of results was performed using the Simulations Interaction Diagram panel along with trajectory analysis. The three-dimensional structures of the screened hit compounds were sketched using GaussView 6.0, followed by their full geometry optimization with the aid of the Gaussian 16 software suite utility[54–56] All calculations were computed in the gas phase using the B3LYP functional, employing B3LYP/6-311 + + G(d, p) basis set[57] and empirical dispersion (GD3). To ascertain that the optimized geometrical configurations represented the true local minima on the potential energy surface, vibrational frequency analyses were performed. In addition to structural data, electronic properties were explored through the calculation of frontier molecular orbitals (FMOs), specifically the highest occupied molecular orbital (HOMO) and the lowest unoccupied molecular orbital (LUMO). These orbitals are of significant value to assess notable quantum chemical descriptors such as chemical reactivity, electrophilicity, chemical softness, chemical hardness, electron affinity and ionization potential, which were derived from the HOMO/LUMO energy gap (ΔE)[55,58]. To further seek out molecular potential regions likely to engage in electrophilic or nucleophilic attacks, Molecular Electrostatic Potential (MEP) maps were also rendered[58,59]. These MEP analyses, analyzed under the same DFT framework, furnished a quantitative and visual apprehension of the electronic landscape surrounding each hit compound.

Post-molecular dynamics simulation analyses

PCA and DCCM analyses
For the assessment of the collective movement of the protein and correlated residues movements, Principal Component Analysis (PCA) and Dynamic cross-correlation matrix (DCCM) analyses were performed using the Bio3D package version 2.4.5[60] in the R programming environment version 4.5.1[61]. Appropriate topology and trajectory conversion (without waters and ions) of the simulation files for the Bio3D acceptable format was obtained through the VMD (Visual Molecular Dynamics) program version 2.0.0a4[62]. Three atom selections were analyzed from MD simulation study, (A) All Cα of protein, (B) binding site residues within 5 Å of 5u ligand (5u's atoms excluded), (C) binding site residues within 5 Å of ligand 5u including the ligand's atoms (total 73

atoms, Cα of residues within 5 Å of 5u, 1–25, ligand atoms 26–73). MDAnalysis version 2.9.0[63,64] was used to calculate the residues within 5 Å distance of the ligand atoms.

Free energy landscape analysis
Free Energy Landscape (FEL) analysis based on the RG-RMSD method was performed to access the energy and stability of the protein-ligand complex using Geo Measures v0.9d[65] plugin in PyMol version 3.1.0 open-source build[66].

α-glucosidase inhibition assay
In recent research, a 50 mM phosphate buffer with a pH of 6.8 was used. Both the enzyme and the substrate were dissolved in this buffer. Furthermore, the experiments used the same buffer as the reaction buffer. Two units of the enzyme were dissolved for every two milliliters of reaction volume. 20 µL of test samples at a concentration of 0.5 mM and 135 µL of the reaction buffer per well were added to the 96-well plate along with this quantity of enzyme, which is equal to 0.02 u per well[67–70]. The 96-well plate was incubated for an additional 15 min at 37 °C. Following the incubation time, each well received 25 µL of the substrate 4-nitrophenyl-α-D-glucopyranoside. Absorbance was measured at 400 nm for 30 min to observe variations caused by the substrate's varying concentrations. 7% DMSO served as the negative control in this experiment, whereas acarbose served as the positive control. Although the general process was the same, various doses of 4-nitrophenyl-α-D-glucopyranoside (substrate) were used to investigate the kinetics of enzyme inhibition (Figs. S51–52).

Statistical analysis
Programs such as Excel and the SoftMax Pro suite were used to examine the obtained findings for biological activity.

The formula below was used to calculate the percent inhibition.

$$\%Inhibition = 100 - \left(\frac{O.D_{test\ compound}}{O.D_{control}}\right) \times 100 \quad (1)$$

For all studied samples, EZ-FIT (Perrella Scientific, Inc., USA) was utilised to calculate the IC50. All experiments were conducted in triplicate to minimise anticipated errors, and Standard Error of Mean values (SEM) are used to represent differences in the results.

$$SE = \frac{\sigma}{\sqrt{n}} \quad (2)$$

Conclusion
In summary, this work introduces a structurally novel series of N-substituted indole-based thiosemicarbazones exhibiting exceptional α-glucosidase inhibitory activity, with all compounds significantly outperforming the standard inhibitor, acarbose. Relative to previously reported inhibitors, these derivatives offer both enhanced potency and unique pharmacophoric architecture, thereby addressing a critical gap in current antidiabetic drug development. Compound **5u**, in particular, demonstrated superior binding affinity and stability within the enzyme active site, as confirmed by molecular docking and dynamic simulation studies. Future work will focus on in vivo validation, pharmacokinetic assessment, and structural optimization to enhance its drug-like properties. These efforts will provide critical insights into the translational potential of this scaffold and support the development of next-generation antidiabetic therapeutics. The quantum chemical descriptors' analysis validates the original steric/electronic SAR hypothesis and explains the significant activity improvements. These parameters not only support the observed potency ranking (**5u** > **5 h** ≈ **5w** > **5s** > others) but also provide predictive guidance for future structural optimization.

Data availability
All data generated or analyzed during this study are included in this published article [and its supplementary information files.

Received: 5 June 2025; Accepted: 13 October 2025
Published online: 06 November 2025

References
1. Saeedi, P. et al. Global and regional diabetes prevalence estimates for 2019 and projections for 2030 and 2045: results from the international diabetes federation diabetes atlas. *Diabetes Res. Clin. Pract.* **157**, 107843 (2019).
2. Szczechla, M., Balewska, A., Naskręt, D., Zozulińska-Ziółkiewicz, D. & Uruska, A. Molecular changes in cells of patients with type 2 diabetes mellitus depending on changes in glycemia level in the context of Lifestyle—An overview of the latest scientific discoveries. *Curr. Issues. Mol. Biol.* **45** (3), 1961–1981 (2023).
3. Committee, A. D. A. P. P. & Committee:, A. D. A. P. P. 2. Classification and diagnosis of diabetes: standards of medical care in Diabetes—2022. *Diabetes Care*. **45** (Supplement_1), S17–S38 (2022).
4. Tancredi, M. et al. Excess mortality among persons with type 2 diabetes. *N. Engl. J. Med.* **373** (18), 1720–1732 (2015).
5. Lawrence, J. M. et al. Trends in prevalence of type 1 and type 2 diabetes in children and adolescents in the US, 2001–2017. *Jama* **326** (8), 717–727 (2021).
6. Kahn, S. E., Cooper, M. E. & Del Prato, S. Pathophysiology and treatment of type 2 diabetes: perspectives on the past, present, and future. *Lancet* **383** (9922), 1068–1083 (2014).
7. Baena-Díez, J. M. et al. Risk of cause-specific death in individuals with diabetes: a competing risks analysis. *Diabetes Care*. **39** (11), 1987–1995 (2016).

8. Al-Maskari, F., El-Sadig, M. & Nagelkerke, N. Assessment of the direct medical costs of diabetes mellitus and its complications in the united Arab Emirates. *BMC public. Health*. **10**, 1–10 (2010).
9. Ye, J. et al. The global, regional and National burden of type 2 diabetes mellitus in the past, present and future: a systematic analysis of the global burden of disease study 2019. *Front. Endocrinol.* **14**, 1192629 (2023).
10. Weinberg Sibony, R., Segev, O., Dor, S. & Raz, I. Drug therapies for diabetes. *Int. J. Mol. Sci.* **24** (24), 17147 (2023).
11. Nyenwe, E. A., Jerkins, T. W., Umpierrez, G. E. & Kitabchi, A. E. Management of type 2 diabetes: evolving strategies for the treatment of patients with type 2 diabetes. *Metabolism* **60** (1), 1–23 (2011).
12. Dirir, A. M., Daou, M., Yousef, A. F. & Yousef, L. F. A review of alpha-glucosidase inhibitors from plants as potential candidates for the treatment of type-2 diabetes. *Phytochem. Rev.* **21** (4), 1049–1079 (2022).
13. Roshan, M., Mirzazadeh, R., Tajmir-Riahi, A. & Asgari, M. S. Rational design, synthesis, in vitro, and in-silico studies of pyrazole–phthalazine hybrids as new α–glucosidase inhibitors. *Sci. Rep.* **15** (1), 3744 (2025).
14. Wang, G. et al. Synthesis, biological evaluation and molecular Docking studies of Chromone hydrazone derivatives as α-glucosidase inhibitors. *Bioorg. Med. Chem. Lett.* **27** (13), 2957–2961 (2017).
15. Mollica, A. et al. Combinatorial peptide library screening for discovery of diverse α-glucosidase inhibitors using molecular dynamics simulations and binary QSAR models. *J. Biomol. Struct. Dynamics*. **37** (3), 726–740 (2019).
16. Hsieh, J. F. et al. Antioxidant activity and Inhibition of α-glucosidase by hydroxyl-functionalized 2-arylbenzo [b] furans. *Eur. J. Med. Chem.* **93**, 443–451 (2015).
17. Ghomi, M. K. et al. Evaluation of novel 2-(quinoline-2-ylthio) acetamide derivatives linked to diphenyl-imidazole as α-glucosidase inhibitors: insights from in silico, in vitro, and in vivo studies on their anti-diabetic properties. *Eur. J. Med. Chem.* **269**, 116332 (2024).
18. Mushtaq, A., Azam, U., Mehreen, S. & Naseer, M. M. Synthetic α-glucosidase inhibitors as promising anti-diabetic agents: recent developments and future challenges. *Eur. J. Med. Chem.* **249**, 115119 (2023).
19. Abuelizz, H. A. et al. Triazoloquinazolines as a new class of potent α-glucosidase inhibitors: in vitro evaluation and docking study. *PLoS ONE* **14** (8), e0220379. (2019).
20. Fan, M., Zhong, X., Huang, Y., Peng, Z. & Wang, G. Synthesis, biological evaluation and molecular Docking studies of Chromone derivatives as potential α-glucosidase inhibitors. *J. Mol. Struct.* **1274**, 134575 (2023).
21. Wang, L. et al. Synthesis and evaluation of Phenyltriazole-Deoxynojirimycin hybrids as potent α-Glucosidase inhibitors. *Molecules* **29** (21), 5062 (2024).
22. Singh, T. P. & Singh, O. M. Recent progress in biological activities of Indole and Indole alkaloids. *Mini Rev. Med. Chem.* **18** (1), 9–25 (2018).
23. Locock, K. E. et al. Antimicrobial polymethacrylates synthesized as mimics of tryptophan-rich cationic peptides. *ACS Macro Lett.* **3** (4), 319–323 (2014).
24. Singh, R. V., Rana, L. & Bendi, R. A. Chemistry of quinoline based heterocycle scaffolds: a comprehensive review. *ChemistrySelect* **7** (46), e202203648. (2022).
25. Islam, M. S. et al. Catalytic asymmetric synthesis of Indole derivatives as novel α-glucosidase inhibitors in vitro. *Bioorg. Chem.* **79**, 350–354 (2018).
26. Khan, M. et al. Discovery of novel oxindole derivatives as potent α-glucosidase inhibitors. *Bioorg. Med. Chem.* **22** (13), 3441–3448 (2014).
27. Kawde, A. N. et al. Exploring efficacy of indole-based dual inhibitors for α-glucosidase and α-amylase enzymes: in silico, biochemical and kinetic studies. *Int. J. Biol. Macromol.* **154**, 217–232 (2020).
28. Solangi, M. et al. Indole acrylonitriles as potential anti-hyperglycemic agents: Synthesis, α-glucosidase inhibitory activity and molecular Docking studies. *Bioorg. Med. Chem.* **28** (21), 115605 (2020).
29. Sharma, P., Gupta, G. & Asati, V. Design, synthesis and antidiabetic study of Triazole clubbed Indole derivatives as α-glucosidase inhibitors. *Bioorg. Chem.* **139**, 106750 (2023).
30. Altunoluk, O. C., Özbek, O., Kalay, E., Tokalı, F. S. & Aslan, O. N. Surface characterization of barium (II)-selective potentiometric sensor based on a newly synthesized thiosemicarbazone derivative molecule. *Electroanalysis* **36** (7), e202300407. (2024).
31. Batool, Z. et al. Design, synthesis, and in vitro and in Silico study of 1-benzyl-indole hybrid thiosemicarbazones as competitive tyrosinase inhibitors. *RSC Adv.* **14** (39), 28524–28542 (2024).
32. Batool, Z. et al. N-hexylsulfonyl indole based thiosemicarbazones as potent and selective ecto-5′-nucleotidase and NTPDase inhibitors. *Bioorg. Chem*. 108717. (2025).
33. Manaf, A. et al. Characterization and antioxidant activities of semicarbazide and thiosemicarbazide derivatives. *J. Chem. Soc. Pakistan* **43** (4). (2021).
34. Jacob, Í. T. et al. Anti-inflammatory activity of novel thiosemicarbazone compounds indole-based as COX inhibitors. *Pharmacol. Rep.* **73**, 907–925 (2021).
35. Shakya, B. & Yadav, P. N. Thiosemicarbazones as potent anticancer agents and their modes of action. *Mini Rev. Med. Chem.* **20** (8), 638–661 (2020).
36. Kaplancıklı, Z. A., Altıntop, M. D., Sever, B., Cantürk, Z. & Özdemir, A. Synthesis and in vitro evaluation of new thiosemicarbazone derivatives as potential antimicrobial agents. *J. Chem.* **2016** (1), 1692540. (2016).
37. Batool, Z. et al. Design, synthesis, QSAR modelling and molecular dynamic simulations of N-tosyl-indole hybrid thiosemicarbazones as competitive tyrosinase inhibitors. *Sci. Rep.* **14** (1), 25754 (2024).
38. Rasool, A. et al. Bis-pharmacophore of cinnamaldehyde-clubbed thiosemicarbazones as potent carbonic anhydrase-II inhibitors. *Sci. Rep.* **12** (1), 16095 (2022).
39. Kim, S. J. et al. Bioprinting methods for fabricating in vitro tubular blood vessel models. *Cyborg Bionic Syst.* **4**, 0043 (2023).
40. Pasha, A. R. et al. Synthesis, in vitro α-glucosidase inhibitory potential and in Silico study of 2–chloro pyridine incorporated thiosemicarbazones. *J. Mol. Struct.* **1317**, 139089 (2024).
41. Islam, M. et al. Design, synthesis, in vitro, and in Silico studies of 4-fluorocinnamaldehyde based thiosemicarbazones as urease inhibitors. *Sci. Rep.* **15** (1), 609 (2025).
42. Tokalı, F. S., Taslimi, P., Usanmaz, H., Karaman, M. & Şendil, K. Synthesis, characterization, biological activity and molecular Docking studies of novel schiff bases derived from thiosemicarbazide: biochemical and computational approach. *J. Mol. Struct.* **1231**, 129666 (2021).
43. Kang, L. et al. Structure–activity relationship investigation of coumarin–chalcone hybrids with diverse side-chains as acetylcholinesterase and butyrylcholinesterase inhibitors. *Mol. Diversity*. **22**, 893–906 (2018).
44. Tokalı, F. S. et al. Synthesis of new carboxylates and sulfonates containing thiazolidin-4-one ring and evaluation of inhibitory properties against some metabolic enzymes. *J. Iran. Chem. Soc.* **20** (10), 2631–2642 (2023).
45. Ullah, W. et al. Synthesis of Indole based sulfonamide derivatives as potent inhibitors of α-glucosidase and α-amylase in management of type-II diabetes. *Chem. Data Collections*. **50**, 101122 (2024).
46. Hu, C. et al. Synthesis and biological evaluation of Indole derivatives containing thiazolidine-2, 4-dione as α-glucosidase inhibitors with antidiabetic activity. *Eur. J. Med. Chem.* **264**, 115957 (2024).
47. Ullah, A. et al. Synthesis of new indole-Based thiazole derivatives as potential antiglycation and anti α-Glucosidase agents: in vitro and in Silico studies. *ChemistrySelect* **8** (47), e202301884 (2023).
48. Gul, S. et al. Discovering the anti-diabetic potential of thiosemicarbazone derivatives: in vitro α-glucosidase, α-amylase inhibitory activities with molecular Docking and DFT investigations. *J. Mol. Struct.* **1312**, 138671 (2024).

49. Zahra, S. B. et al. Synthesis of novel coumarin-based thiosemicarbazones and their implications in diabetic management via in-vitro and in-silico approaches. *Sci. Rep.* **13** (1), 18014 (2023).
50. Ni, X., Luo, X., Jiang, X., Chen, W. & Bai, R. Small-Molecule tyrosinase inhibitors for treatment of hyperpigmentation. *Molecules* **30** (4), 788 (2025).
51. Chaudhry, F. et al. A. In search of new α-glucosidase inhibitors: Imidazolylpyrazole derivatives. *Bioorg. Chem.* **71**, 102–109 (2017).
52. Release, S. *4: Desmond Molecular Dynamics System*. (DE Shaw Research, 2017).
53. Bashir, M., Abdullah, U., Siddique, F. & Jalal, N. Computational advances in the design and discovery of Artemis inhibitors for radiosensitization in cancer therapy. *Front. Chem.* **13**, 1597454 (2025).
54. Abida Ejaz, S. et al. Computational exploration of fluorocyclopentenyl-purines and-pyrimidines derivatives as potential inhibitors of epidermal growth factor receptor (EGFR) for the treatment of breast cancer. *Chem. Biodivers.* **20** (12), e202301190. (2023).
55. Bashir, M. et al. Computational insights into Structural, optoelectronic and charge transfer properties of monocarbonyl Curcumin derivatives for biomedical and photonic applications. *J. Comput. Biophys. Chem.* **25** (2), 185–211 (2026).
56. Wajid, M. et al. Synthesis, biological Assessment, and computational analysis of sulfathiazole schiff bases. *J. Comput. Biophys. Chem.* **25** (6), 893–917 (2026).
57. Tirado-Rives, J. & Jorgensen, W. L. Performance of B3LYP density functional methods for a large set of organic molecules. *J. Chem. Theory Comput.* **4** (2), 297–306 (2008).
58. Naseer, I. et al. Antidiabetic assessment, metal chelating impacts, and computational modeling of 4-fluorophenyl sulfonyl-indole based hydrazones. *J. Mol. Struct.* 143878. (2025).
59. Sheikhi, M., Balali, E. & Lari, H. Theoretical investigations on molecular structure, NBO, HOMO-LUMO and MEP analysis of two crystal structures of N-(2-benzoyl-phenyl) oxalyl: A DFT study. *J. Phys. Theoretical Chem.* **13** (2), 155–169 (2016).
60. Grant, B. J., Rodrigues, A. P., ElSawy, K. M., McCammon, J. A. & Caves, L. Bio3d: an R package for the comparative analysis of protein structures. *Bioinformatics* **22** (21), 2695–2696 (2006).
61. Team, R. C. *R: A Language and Environment for Statistical Computing*. (R Foundation for Statistical Computing, 2016).
62. Humphrey, W., Dalke, A. & Schulten, K. VMD: visual molecular dynamics. *J. Mol. Graph.* **14** (1), 33–38 (1996).
63. Gowers, R. J. et al. *MDAnalysis: a Python Package for the Rapid Analysis of Molecular Dynamics Simulations* (Los Alamos National Laboratory (LANL), 2019).
64. Michaud-Agrawal, N., Denning, E. J., Woolf, T. B. & Beckstein, O. MDAnalysis: a toolkit for the analysis of molecular dynamics simulations. *J. Comput. Chem.* **32** (10), 2319–2327 (2011).
65. Kagami, L. P., das Neves, G. M., Timmers, L. F. S. M., Caceres, R. A. & Eifler-Lima, V. L. Geo-Measures: A PyMOL plugin for protein structure ensembles analysis. *Comput. Biol. Chem.* **87**, 107322 (2020).
66. Schrodinger, L. The PyMOL molecular graphics system. *Version* **1**, 8 (2015).
67. Jenis, J. et al. Competitive α-glucosidase inhibitors, dihydrobenzoxanthones, from the barks of Artocarpus elasticus. *J. Enzyme Inhib. Med. Chem.* **34** (1), 1623–1632 (2019).
68. Basri, R. et al. Synthesis, biological evaluation and molecular modelling of 3-Formyl-6-isopropylchromone derived thiosemicarbazones as α-glucosidase inhibitors. *Bioorg. Chem.* **139**, 106739 (2023).
69. Farooqi, R. et al. Design, synthesis, in-vitro and in-silico studies of novel N-heterocycle based hydrazones as α-glucosidase inhibitors. *Bioorg. Chem.* **156**, 108155 (2025).
70. Alharthy, R. D. et al. Synthesis of the chromone-thiosemicarbazone scaffold as promising α-glucosidase inhibitors: an in vitro and in Silico approach toward antidiabetic drug design. *Arch. Pharm.* **357** (8), 2400140 (2024).

Acknowledgements

This work was funded by the Ongoing Research Funding program (ORF-2025-1100), King Saud University, Riyadh, Saudi Arabia. Z.S. is grateful to the Alexander von Humboldt Foundation for the award of Return Fellowship.

Author contributions

I.N. and J.H. designed and synthesized the compounds; S.U. and A.K. performed the enzyme inhibition assay; M.a-R, T.I., and M.S.I. performed molecular modeling studies; A.M.T. carried out characterization and Funding acquisition; Z.S. and A.A-H. supervised the work and wrote the manuscript with the help of Z.B. All authors read and approved the manuscript.

Funding

This work was funded by the Ongoing Research Funding program (ORF-2025-1100), King Saud University, Riyadh, Saudi Arabia.

Declarations

Competing interests

The authors declare no competing interests.

Additional information

Supplementary Information The online version contains supplementary material available at https://doi.org/10.1038/s41598-025-24251-w.

Correspondence and requests for materials should be addressed to A.A.-H., Z.S. or M.S.I.